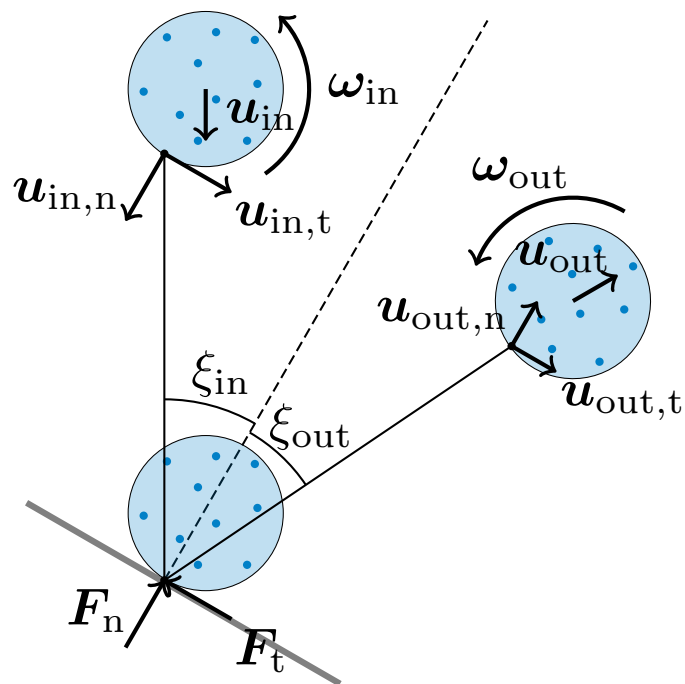


Oblique Particle-Wall Collisions in a Viscous Fluid

– Master Thesis –
P&E 2678 / MEAH 287

July 14, 2015



Lyckle Drost

lyckledrost@gmail.com

Supervisors:

Dr.ir. W.-P. Breugem

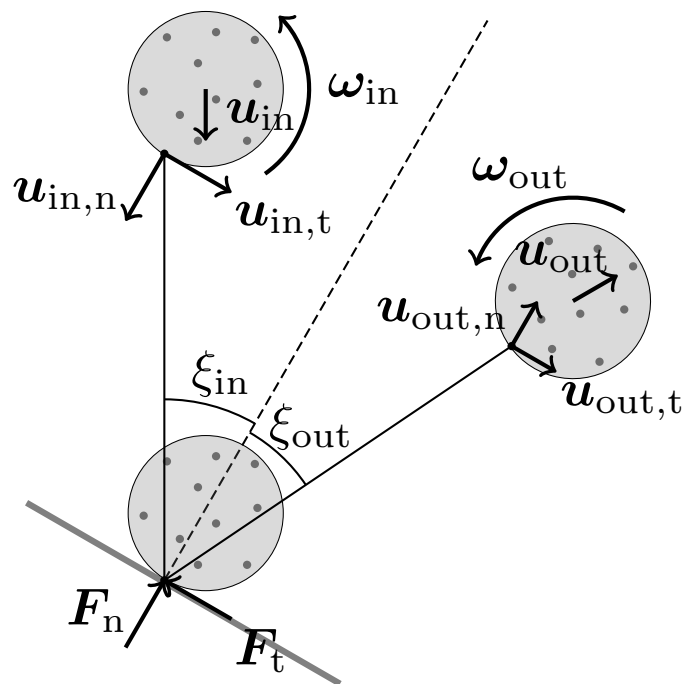
Eng. P. Costa

Dr.ir. C. Poelma

Oblique Particle-Wall Collisions in a Viscous Fluid

– Master Thesis –
P&E 2678 / MEAH 287

July 14, 2015



Lyckle Drost

lyckledrost@gmail.com

Supervisors:

Dr.ir. W.-P. Breugem

Eng. P. Costa

Dr.ir. C. Poelma

Graduation Committee:

Prof.dr.ir. J. Westerweel

Dr.ir. G.H. Keetels

Dr.ir. W.-P. Breugem

Dr.ir. C. Poelma

Eng. P. Costa

Abstract

Interaction of particles in a viscous fluid with a wall and with other particles is often observed in phenomena like sedimentation, erosion and filtration processes. With the increasing computational power there is now the possibility of simulating such particle-laden flows from a micro-scale perspective by direct application of no-slip/no-penetration boundary conditions at the particles' surface. To model the collisions in a particle-laden flow in an realistic manner it is required to understand the dynamics of individual collisions.

To investigate the relevant parameters describing particle-wall interactions, experiments of a spherical particle colliding with an oblique wall have been performed in both air and in water. The measurements were carried out with spherical steel and delrin particles with a radius of 4 and 5 millimeter. The particle dynamics has been investigated by video-capturing the particle's motion (translation and rotation) and the collision with an inclined plate.

Upon collision with a wall energy is dissipated due to the inelastic nature of the contact. Furthermore the particle may stick or slip at the surface depending on the tangential force during impact. Three parameters are used to describe the macroscopic behavior of the collision. The normal coefficient of restitution e_n quantifies the dissipated energy. The tangential coefficient of restitution e_t quantifies the change in the tangential velocity at the point of the particle that collides with the wall. Finally the Coulomb coefficient of sliding friction μ_f is a measure how easily the particle sticks to or slips over the collision plate. These three parameters are sufficient to describe the dynamics of a particle-wall collision in air (dry collision). In a viscous fluid (wet collisions) these parameters are subject to change due to lubrication, piezo-viscous and history-forces. Whether the particle bounces in the fluid depends on the impact Stokes number ($St = \frac{2}{9} \frac{\rho_s R U}{\mu}$), the ratio between particle inertia and viscous forces. The three parameters will be determined using Walton's collision model [Walton, 1993] and are compared to the results found in literature [Gondret et al., 2002; Joseph and Hunt, 2004].

Furthermore, the difference between normal collisions and the normal component of oblique collisions is investigated. The particle's impact Stokes number, has been plotted against the ratio of the normal wet and normal dry coefficient of restitution and compared to the results found by Joseph et al. [2001] and the empirical fit of Legendre et al. [2006]. In agreement with the results from literature we found that the normal component of oblique collisions equals the the results of normal collisions under similar conditions.

The results for oblique particle wall collisions in a viscous fluid presented in this thesis, add to the few data present in literature, by using a different setup. Since the results for both dry and wet collisions are in agreement with the data from literature, this work may be used as validation for the modeling of particle laden flows.

Preface

From the begin of my life as a student I've been interested in "simple" experiments. Therefore a MSc-project on the experimental study of the motion of a particle obliquely colliding onto a planar surface was a natural choice. Although the experiment proved not to be that "simple", with the support of many the data from literature were reproduced. Therefore I would like to thank some people.

First and foremost I would like to thank my supervisors: Wim-Paul Breugem, Pedro Costa and Christian Poelma. For all the input, discussions and help on the theory of oblique particle-wall collisions, the setup of the experiment and the analysis of the results.

Furthermore I am very grateful for the help of the technical staff of the Laboratory for Aero and Hydrodynamics. In particular I would like to thank Edwin Overmars for providing a high speed camera and related equipment for the setup and for helping me to order the delrin particles. Furthermore I would like to thank Jasper Ruijgrok for the building the wedge setup.

For the optical investigation of the particle's surface roughness I would like to thank Sander van Asperen of the Metals Processing, Microstructures and Properties department. Thank you for showing me how to embed the particles in a synthetic resin, how to saw the embedded particles into halves, how to polish the sawed samples and how to investigate the surface roughness under the microscope.

For the investigation of the particle's surface roughness using stylus profilometry I want to thank Roel Mattern and Eugene Straver of the Kavli Nanolab. Thank you for giving me acces to the cleanroom and for giving me the opportunity to independently measure the surface roughness of the particle on the Tencor profilometer.

During my master-project I spend a lot of time in the master student room. Therefore I would like to thank Avinash, Yves and Tim, thanks to you I have had a great time.

Last but not least I would like to thank the reader of this thesis for showing interest in my work. I hope you will experience the same joy as I had in investigating the dynamics of particle-wall collisions.

L.J. Drost
Delft, June 2015

Contents

Abstract	v
Preface	vii
Table of Contents	viii
1 Introduction	1
1.1 Particles in a Flow	1
1.2 Applications	2
1.3 Research goal and outline	3
2 Oblique Particle-Wall Collisions	5
2.1 Equation of Motion	5
2.2 Sedimentation of a Single Sphere in a Stagnant Fluid	6
2.3 Oblique Collision	7
2.3.1 Dry Collisions	7
2.3.2 Wet Collisions	9
3 Methodology	11
3.1 Experimental Setup	11
3.1.1 Calibration	14
3.2 Data Analysis	14
3.2.1 Position of Sphere & Markers	14
3.2.2 Tracking the Particle Motion	15
4 Results	19
4.1 Dry collisions	19
4.2 Wet collisions	21
4.2.1 Coefficient of restitution	22
5 Conclusions	25

A Particle Surface Roughness	27
A.1 Method	27
A.1.1 Optical	27
A.1.2 Stylus	27
A.2 Results	29
A.2.1 Steel Particles	29
A.2.2 Delrin Particles	30
A.2.3 Glass Surface	32
B Kabsch Algorithm	33
B.1 Theory and Propagation of Uncertainties	34
B.1.1 Theory	34
B.1.2 Analytical Analysis of Error Propagation	36
B.1.3 Numerical Analysis of Error Propagation	38
B.2 Results	41
B.2.1 Influence of perturbations	41
B.2.2 Summary	45
B.3 Conclusion	46
Bibliography	47

1 Introduction

This chapter gives the motivation for the research presented in this thesis. We start with a brief discussion of particle-particle and particle-wall interactions in a flow. Subsequently, Section 1.2 gives a brief overview of phenomena observed in nature and in industrial applications. Finally Section 1.3 presents the research goal and outline of the thesis.

1.1 Particles in a Flow

In wall-bounded particle-laden flows, particles may interact with each other and with a wall, as illustrated in Figure 1.1. Particles may roll (A) or slide (B) over the surface but can also be suspended in the flow (D). In some cases, particles are lifted from the bed and dragged along with the flow before returning to the ground, thereby eventually ejecting other particles in the flow [Shields, 1936; Durán et al., 2012]. This process is called saltation (C). These processes are highly dependent on the particle properties such as size, shape, density, roughness and stiffness and the local flow dynamics. The local flow dynamics is dependent on the fluid properties like density and viscosity but also on the particle volume fraction which

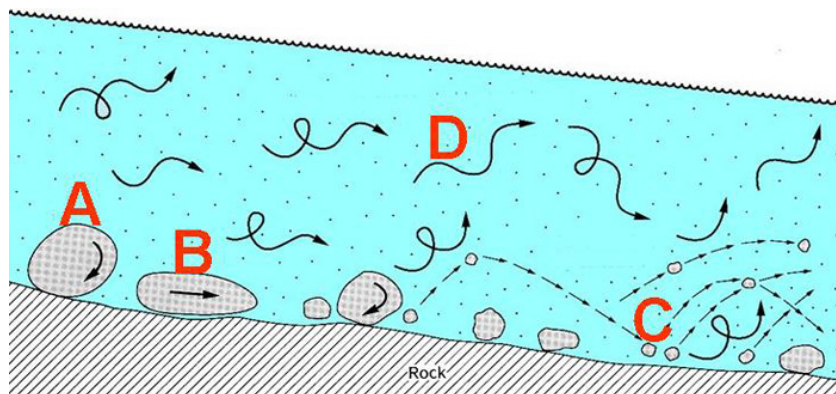


Figure 1.1: Sediment transport in a river bed. For creeping motion in which the particle remains at the surface, the particle may roll (A) or slide (B) over the bed. Saltating behavior (C), particles may be lifted from the bed and dragged along with the fluid before returning to the bed thereby eventually launching other particles from the bed. Suspended particles (D) are carried along with the bulk flow. Next to the particle and fluid properties, the dynamics of the particle is dependent on the local flow dynamics. Figure by Karina Molfa (<http://brasil.cel.agh.edu.pl/~10skmolfa/galeria>).

may change the rheology of the flow [Morris, 2009].

The behavior of particles in a flow described above is often observed in applications like sedimentation, erosion and filtration processes. With increasing computational power there is now the possibility of modeling such particle-laden flows [Derksen, 2011; Kempe et al., 2014], for instance with an immersed boundary method [Breugem, 2012; Costa et al., 2015]. To do this in a realistic manner it is mandatory to understand the dynamics of individual collisions [Davis et al., 1986; Barnocky and Davis, 1989; Joseph et al., 2001; Joseph and Hunt, 2004; Legendre et al., 2006]. When a particle with a nonzero tangential velocity collides with a wall, the particle may stick to or slip over the surface, dependent on the tangential force during impact. In a viscous fluid, lubrication, piezo-viscous [Barnocky and Davis, 1989] and history forces [Gondret et al., 2002] cannot be neglected. Next to the understanding of individual collisions, there is a need for accurate experimental data for validation of the collision models. This thesis is therefore dedicated to the experimental investigation of oblique particle-wall collisions.

1.2 Applications

Particle-laden flows appear in a wide range of natural and industrial contexts. Examples are aeolian transport, i.e. transport in air, which is observed in desert areas, as shown in Figure 1.2. In this case the medium is such that short-range hydrodynamic interactions such as lubrication forces are negligible. Among this category are also drift-sands on the beach or drifting ice/snow particles during winter.

There are also examples where the medium is a viscous liquid such as water.



Figure 1.2: Aeolian transport of sand from a crest in the Kelso Dunes of the Mojave Desert, California. Photograph taken by Mark A. Wilson (Department of Geology, The College of Wooster), en.wikipedia.org.



Figure 1.3: Coastal reinforcement near The Hague by application of rainbowing. In this process the sand-water mixture is collected from the sea-floor and transported to the coastal region. The rainbowing process allows deposition of the slurry in shallow water areas. Figure taken from “Beeldbank Rijkswaterstaat”.

In water one usually speaks about sedimentation or sediment transport. In sedimentation, the suspended particles move towards a wall where they come at rest. This process is for instance used for the purification of drinking water and sewage treatment.

Another example is the dredging industry, which deals with the transport of sand-water mixtures, called slurry, through pipes. This is for instance done in regions where coastal areas have to be reinforced or where new land has to be claimed from the sea such as the Palm Islands near Dubai. Sand is usually collected from the sea-floor. The fluid properties of the slurry, which is dependent on the particle concentration, allows deposition by a technique called rainbowing, as shown in Figure 1.3.

1.3 Research goal and outline

The objective of this thesis is to experimentally investigate the hydrodynamic interaction of a spherical particle colliding obliquely onto a planar surface. Starting from the equations of motion for both the fluid and dispersed phase, the equation of motion for a single particle in a stagnant fluid is derived in Section 2.2. Upon collision with a wall, the energy dissipation due to the inelastic nature of the solid-solid contact has to be taken into account. Section 2.3.1 presents Walton’s three-parameter model which has been used to describe the collision process. In a viscous liquid these parameters are subject to change due to lubrication- and piezo-viscous forces as will be outlined in Section 2.3.2.

Chapter 3 starts with a description of the physical parameters describing the particles, fluids and the target plate, followed by the description of the experimental setup. Appendix A gives an elaborate discussion on the procedures used to measure the roughness of the particles and collision plate. Section 3.2 explains the data analysis and is divided in two parts. First, the detection of the position of the sphere and the markers, which are used to track the particle's rotation, is discussed in Section 3.2.1. Section 3.2.2 discusses how the rotation of the particle is derived from the position of the markers. Furthermore this section discusses the detection of the moment of collision and the procedure to find the normal- and tangential velocity prior to and just after the collision. In close relation to Chapter 3, Appendix B gives an elaborate discussion on the Kabsch algorithm, which is used to find the rotation of the particle from the positions of the markers. Besides the mathematical background, the influence of the uncertainties in the positions of the markers on the rotation found, is investigated analytically and numerically.

The experimental results are presented in Chapter 4, following the theoretical analysis of Chapter 2. The results of the dry collisions for the separate parameters of Walton's three-parameter model are plotted against the incidence angle in Section 4.1. Section 4.2 shows the results for the wet collisions. Finally we confirm the self-similar dependency of the ratio between the normal wet coefficient of restitution to the normal dry coefficient of restitution as function of Stokes number based on the normal impact velocity.

Chapter 5 concludes the findings of the results chapter and presents recommendations for further experiments.

2 Oblique Particle-Wall Collisions

The motion of particles in a fluid is governed by the coupling of the equations of motion for the continuous and dispersed phase. The fluid phase is described by the Navier-Stokes equations and the solid phase by the Newton-Euler equations. This chapter starts with an overview of these equations (Section 2.1). Subsequently, Section 2.2 gives the equation of a single sphere sedimenting in a quiescent fluid. This chapter concludes with the theory for oblique particle wall collisions, starting with dry collisions in Section 2.3.1. In a viscous (wet) fluid, lubrication, piezo-viscous and history-forces cannot be neglected as will be discussed in Section 2.3.2.

2.1 Equation of Motion

The dynamics of a spherical particle in a viscous fluid are described by the coupling of the equations of motion for the fluid phase and the dispersed phase. The fluid phase, for an incompressible Newtonian fluid, is described by the continuity- and Navier-Stokes equations

$$\nabla \cdot \mathbf{u}_f = 0, \quad (2.1a)$$

$$\rho_f \left(\frac{\partial \mathbf{u}_f}{\partial t} + (\mathbf{u}_f \cdot \nabla) \mathbf{u}_f \right) = -\nabla p + \mu_f \nabla^2 \mathbf{u}_f. \quad (2.1b)$$

The motion of a spherical particle is described by the Newton-Euler equations

$$\frac{d\mathbf{p}}{dt} = \oint_{\Gamma} \boldsymbol{\sigma} \cdot d\boldsymbol{\Gamma} + \mathbf{F}, \quad (2.2a)$$

$$\frac{d\mathbf{L}}{dt} = \oint_{\Gamma} (\mathbf{x} - \mathbf{x}_p) \times (\boldsymbol{\sigma} \cdot d\boldsymbol{\Gamma}) + \mathbf{M}, \quad (2.2b)$$

where $\mathbf{p} = m_p \mathbf{u}_p$ and $\mathbf{L} = I_p \boldsymbol{\omega}_p$ are the the particle's linear and angular momentum, respectively.

Two-way coupling can be done through the imposition of no-slip and no-penetration boundary conditions at the surface of the sphere. For sufficiently small particles in the Stokes regime the coupling results into the Maxey-Riley-Gatignol equations [Maxey and Riley, 1983; Gatignol, 1983].¹ Otherwise, velocity-

¹The derivations of the equation of motion by Maxey & Riley and Gatignol were published almost simultaneously. At present, the Maxey-Riley equation is the most cited theory of the two in literature, but is restricted to linear momentum. The derivation by Gatignol also contains the rotational motion and therefore is more complete [Warncke, 2014].

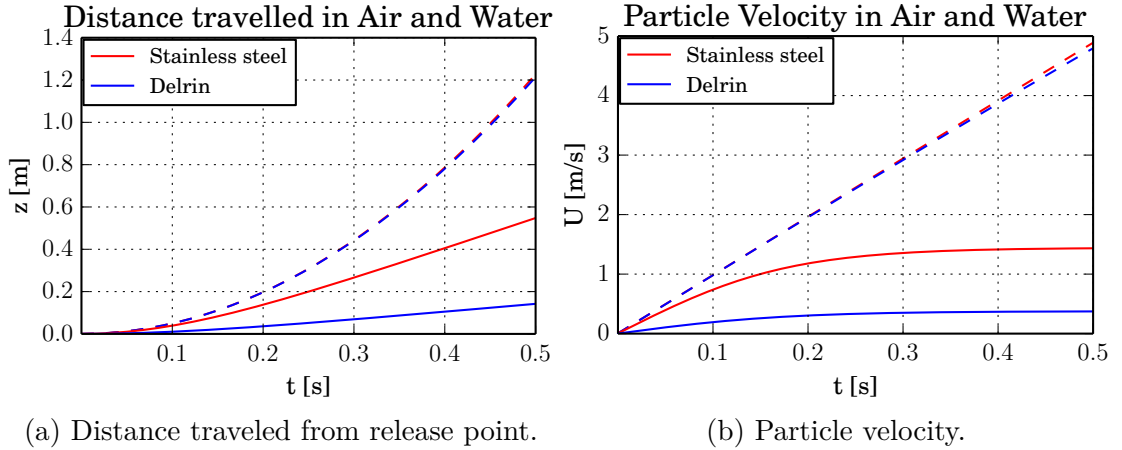


Figure 2.1: Traveled distance and velocity as function of time for $R = 5$ mm steel and delrin particles falling through air (dashed lines) and water (solid lines). The results are obtained by numerical integration of Equation 2.3 using an Euler forward scheme. Material properties of the particles and the fluids can be found in Tables 3.1 and 3.3 respectively.

dependent correlations have to be used for the drag-, lift- and history-forces acting on the particle [Crowe et al., 2011].

Interactions among particles (four-way coupling) or particles and walls are accounted for by external forces, e.g. collision, lubrication and piezo-viscous forces, appearing in \mathbf{F} and \mathbf{M} in the Newton-Euler equations (2.2).

2.2 Sedimentation of a Single Sphere in a Stagnant Fluid

The equation of motion for a single sphere, sedimenting in a quiescent fluid, is given by [Crowe et al., 2011]

$$\underbrace{\rho_p V_p \frac{d\mathbf{u}}{dt}}_{\text{particle inertia}} = - \underbrace{\frac{1}{2} C_D \rho_f \pi R^2 |\mathbf{u}| \mathbf{u}}_{\text{drag force}} - \underbrace{\frac{\rho_f V_p}{2} \frac{d\mathbf{u}}{dt}}_{\text{added mass}} + \underbrace{(\rho_p - \rho_f) V_p \mathbf{g}}_{\text{buoyancy}}, \quad (2.3)$$

where $C_D = C_D(\mathbf{u})$ the drag coefficient dependent on the particle's slip velocity \mathbf{u} [Subramanian, 2010]. Figure 2.1 shows the particle's velocity and trajectory, obtained by numerical integration of Equation 2.3, of a particle falling through air and water. From this figure one observes that, due to the smaller particle-fluid density ratio, the settling velocity in water is reached much earlier than in air.

2.3 Oblique Collision

When a particle collides with a wall, energy is dissipated due to the inelastic nature of the contact mechanics. This inelasticity can be quantified by a normal coefficient of restitution,

$$e_n = \frac{u_{n,\text{out}}}{u_{n,\text{in}}}, \quad (2.4)$$

which is the ratio of the rebound to the impact velocity. If the impact angle ξ_{in} , as shown in Figure 2.2 is nonzero, the collision is oblique. In this case the dynamics of the particle after collision is dependent on the tangential force during impact, which can be characterized by the Coulomb coefficient of sliding friction μ_c and both the tangential and normal coefficient of restitution e_t and e_n .

2.3.1 Dry Collisions

Let us consider an oblique particle-wall collision in air, which we will refer to as a dry collision, as shown in Figure 2.2. In this case all forces in Equation 2.3 except gravity are negligible. For convenience we define the effective angles of incidence and rebound as follows:

$$\Psi_{\text{in}} = \left| \frac{u_{\text{in},t}}{u_{\text{in},n}} \right| = \tan(\xi_{\text{in}}) \quad \text{and} \quad \Psi_{\text{out}} = \frac{u_{\text{out},t}}{|u_{\text{in},n}|} = e_{n,d} \tan(\xi_{\text{out}}). \quad (2.5)$$

In these equations the subscripts n and t denote the normal and tangential component of the velocity, respectively. The normal and tangential coefficient of restitution are defined by

$$e_{n,d} \equiv \left| \frac{u_{\text{out},n}}{u_{\text{in},n}} \right| \quad \text{and} \quad e_{t,d} \equiv -\frac{u_{\text{out},t}}{|u_{\text{in},t}|}. \quad (2.6)$$

Based on Hertzian contact theory, numerical simulations of Maw et al. [1976] show that three different types of impact may occur. These depend on the value of the normalized incidence angle

$$\psi_{\text{in}} = \frac{2(1-\nu)}{\mu_c(2-\nu)} \Psi_{\text{in}} \quad \left(\text{analogously } \psi_{\text{out}} = \frac{2(1-\nu)}{\mu_c(2-\nu)} \Psi_{\text{out}} \right), \quad (2.7)$$

and a material- and geometry-dependent parameter,

$$\chi = \frac{(1-\nu)(1+1/K^2)}{2-\nu}. \quad (2.8)$$

In these equations ν is the Poisson's ratio and K is the radius of gyration normalized by the particle radius; $K^2 = 2/5$ for a homogeneous solid sphere. The different regimes can be characterized by the three different regions of Figure 2.3:

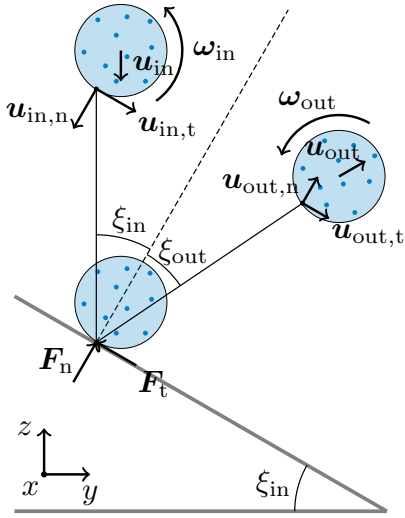


Figure 2.2: Schematic representation of an oblique particle-wall collision. The forces F_n and F_t respectively denote the normal and tangential force during the particle-wall collision.

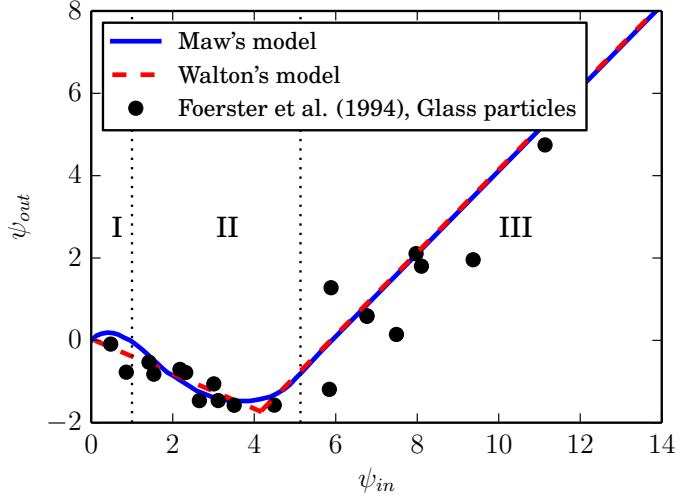


Figure 2.3: The collision models of Maw et al. [1976] and Walton [1993]. The vertical lines denote the different collision regimes bounded by $\psi_{in} = 1$ and $\psi_{in} = 4\chi - 1$. The black dots indicate the, rescaled with $\nu = 0.22$ and $\mu_c = 0.092$ by Costa et al. [2015], experimental results for dry collisions between glass spheres from Foerster et al. [1994].

I. $\psi_{in} \leq 1$: Full stick

The normal component of the load is much larger than the tangential component, consequently the particle sticks to the surface. Regions of micro-slip, slip occurring at the boundary of the contact area, may occur upon decrease of the contact area due to elastic recovery.

II. $1 < \psi_{in} \leq 4\chi - 1$: Gross slip \rightarrow Stick

The tangential component of the load initially dominates during impact but decreases quickly due to frictional stresses. As a result the particle finally sticks in the entire contact area.

III. $\psi_{in} > 4\chi - 1$: Gross slip

The tangential component of the load is so large that gross slip occurs during the entire contact time.

Walton [1993] proposes a simpler 3-parameter model which consists only of a full stick and a gross slip regime. The model makes use of the normal and tangential coefficient of restitution $e_{n, \text{dry}}$ and $e_{t, \text{dry}}$ respectively, and the Coulomb coefficient of sliding friction μ_c . From the latter coefficient the tangential component of the contact force in the gross slip regime is found, i.e.

$$|F_t| = \mu_c |F_n|, \quad (2.9)$$

where $|F_n|$ is the normal component of the contact force. Walton's model represents oblique collisions by two lines in the $\Psi_{\text{in}}, \Psi_{\text{out}}$ plane:

$$\Psi_{\text{out}} = \begin{cases} -e_{t,d}\Psi_{\text{in}} & \Psi_{\text{in}} \leq \Psi_{\text{in}}^* \quad \text{Stick} \\ \Psi_{\text{in}} - \mu_c(1 + 1/K^2)(1 + e_{n,d}) & \Psi_{\text{in}} > \Psi_{\text{in}}^* \quad \text{Slip} \end{cases}, \quad (2.10)$$

where $\Psi_{\text{in}}^* = \mu_d \frac{7}{2} \frac{1+e_{n,d}}{1+e_{t,d}} \Rightarrow \psi_{\text{in}}^* = \Psi_{\text{in}}^* \frac{2(1-\nu)}{\mu_c(2-\nu)}$, based on the continuity of Ψ_{out} at Ψ_{in}^* . Although Walton's model is less sophisticated than Maw's model, both models are in agreement with experimental results [Foerster et al., 1994; Joseph and Hunt, 2004] as shown in Figure 2.3. Since the micro-scale contact mechanics is not resolved in our experiments, the macroscopic description of Walton will be used to determine the three parameters describing the collision.

2.3.2 Wet Collisions

Lubrication effects become important when a particle moving in a viscous fluid approaches another particle or wall closely. In the vicinity of the wall, if $\text{Re}_\delta \ll 1$ and $\delta \ll R$, a lubrication force [Brenner, 1961] needs to be added to the right hand side of the equation of motion (2.3):

$$F_L = -\frac{6\pi\mu_f R^2 u_n}{\delta} \quad (2.11)$$

where δ is the minimum separation distance between the wall and the particle's surface and u_n the particle's normal velocity. The addition of this force to the right hand side of Equation 2.3 leads to the paradox that the particle can never have physical contact with the wall during the collision. For a decreasing particle-wall separation δ the lubrication force namely diverges. In such an elasto-hydrodynamic (EHD) collision fluid always remains in the gap between the particle and the wall. Where fluid is squeezed out of the gap between particle and wall upon incidence, fluid has to be sucked in during rebound. Therefore the lubrication force needs to be taken into account if the particle is in the vicinity of the wall.

Upon rebound the particle enters its own wake. Gondret et al. [Gondret et al., 2002] showed that, for normal collisions in a viscous fluid, a history force therefore cannot be neglected during the collision process.

As discussed by Davis et al. [1986] a decreasing particle-particle separation during an EHD-collision leads to a pressure increase in the gap between the particles. This pressure increase causes the particles' surface to deform till the particle's kinetic energy is converted into elastic strain energy. Their analysis shows that the maximum particle deformation and rebound velocity is dependent on the particle's Stokes impact number

$$\text{St} = \frac{2}{9} \frac{\rho_p R u_n}{\mu_f} = \frac{\text{Re}_D \rho_p}{9 \rho_f}, \quad (2.12)$$

which can be interpreted as the ratio between particle inertia and viscous forces.

For small Stokes numbers viscous effects dominate during the approach of the particle to the wall and the particle does not deform. At large Stokes numbers the collision is governed by the elastic deformation of the particle.

Experimental results, e.g. [Gondret et al., 1999; Joseph et al., 2001; Gondret et al., 2002; Legendre et al., 2006], show that for $St \lesssim 10$ no rebound occurs. For higher Stokes impact the coefficient of restitution asymptotically increases to the dry coefficient of restitution. Legendre et al. [2005] found that the following equation describes well the relation between the effective coefficient of restitution and the particle Stokes number for droplet collisions:

$$\frac{e_{n,w}}{e_{n,d}} = \exp\left(-\frac{\beta}{St}\right), \quad (2.13)$$

where β depends on the Capillary number and the Weber number. For solid spheres, $\beta = 35$ proves to be a good estimate [Legendre et al., 2006].

Although in an ideal EHD-collision smooth spheres never touch the wall, physical contact may take place through the asperities of the particles. For EHD-collisions the closest distance of approach between particle and plate is given by [Davis et al., 1986]:

$$h_{eh} = \left(4\mu_f\theta u_n R^{3/2}\right)^{2/5}, \quad \text{with} \quad \theta = \frac{1-\nu_1^2}{\pi E_1} + \frac{1-\nu_2^2}{\pi E_2}, \quad (2.14)$$

where $\nu_{1,2}$ and $E_{1,2}$ are the Poisson's ratios and Young's moduli of the particle and the wall, respectively. This results in an increasing gap-width for higher normal impact velocity. However, for higher impact velocities piezo-viscous effects (the increase of the fluid-viscosity in the gap between particle and wall upon the increasing pressure and density) become important. Barnocky and Davis [1989] derived a piezo-viscous length scale

$$h_{pv} = \sqrt{\hat{\eta}_f \mu_f u_n R} \quad (2.15)$$

where $\hat{\eta} \approx 10^{-9} \text{ Pa}^{-1}$ is a pressure-viscosity coefficient and μ_f the viscosity at the reference pressure. If $h_{pv} > h_{eh}$ piezo-viscous effects have to be taken into account.

If the size of the asperities is larger than the gap-width between the particle and the wall, collision occurs through the roughness elements [Barnocky and Davis, 1988; Joseph et al., 2001; Joseph and Hunt, 2004]. As outlined by Joseph and Hunt [2004] this results in solidification of the fluid trapped in the asperities between the particle and the wall. As a result the coefficient of sliding friction increases to a level slightly above the coefficient of sliding friction for dry collisions. If particles are smooth, i.e. $\sigma < h_{eh}$, the lubrication layer causes the coefficient of sliding friction to be an order of magnitude lower than for the dry collisions.

3 Methodology

This chapter is dedicated to the experimental setup, materials used and the analysis of the data. The experiment concerns particles falling under the influence of gravity through a (viscous) fluid bouncing on an inclined plate. Details of the setup, particles, impact surface and fluids used for the experiment will be discussed in section 3.1. Section 3.2 treats the analysis of the recorded images to describe the particle motion.

3.1 Experimental Setup

Collision experiments were performed in a glass aquarium, with dimensions $l \times w \times h = 25 \times 25 \times 50$ cm, using steel and delrin spheres² impacting on an inclined glass plate. The experimental setup and particles used are shown in Figure 3.2 and 3.3, respectively. The particles were released with negligible initial rotation from a vacuum tube by turning off the vacuum pump. The impact surface is placed at an angle using perspex wedges of several lengths. Experiments have been carried out both in air (dry collisions) and in water (wet collisions). Tables 3.1, 3.2 and 3.3 give an overview of the specifications of the particles, impact surface and fluids used.

To find the rotation of the particles after impact, markers were applied manually using a permanent marker. A Tencor stylus profilometer was used to measure the particle's surface roughness σ and the local enhancement of the roughness due to addition of the markers. An optical investigation gave similar results for the roughness of the particles. These results are shown in Figure 3.1. A more elaborate discussion on the particle surface roughness including the results from the stylus profilometry is given in Appendix A. The roughness of the particles is shown in Table 3.1. For delrin spheres no influence of the markers on the surface topology was observed. The thickness of the markers on the steel sphere, applied with a different (white) pencil, was measured to be approximately $20 \mu\text{m}$. Hence, markers were only applied to the frontal area of the particle, with respect to the viewpoint of the camera, to avoid anomalous results due to collisions on the markers. The roughness of the glass collision plate, shown in Table 3.2, was only measured using the stylus profilometer.

²Collision experiments with glass spheres were also performed. Due to a large shadow which changed position during the dry measurements it was not possible to track the rotation of the particle. For the wet case the shadow was nearly absent, so the particle nearly vanished in the background. As a result, stable tracking of the particle motion was not possible. As a consequence the post-processing glass dataset is omitted from this report.

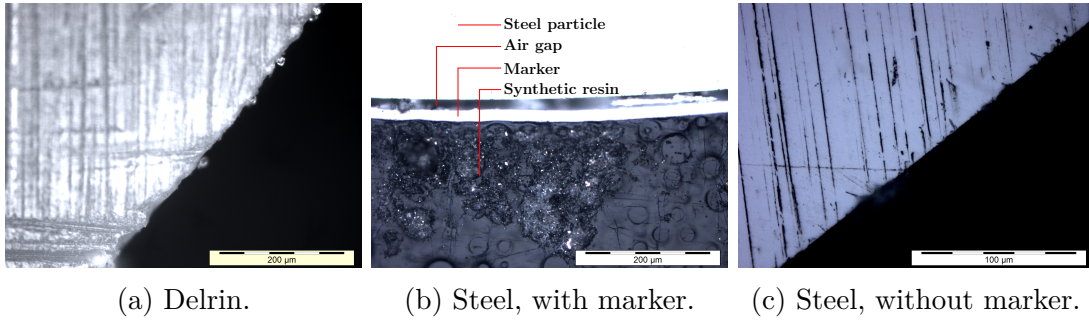


Figure 3.1: Optical investigation of the edge of a half-sphere embedded in a synthetic resin. The lines visible on the particles are due to the polishing process after cutting the particles in halves and have a separation of at least one micrometer. The delrin particle (a) has a surface roughness of micrometer size, and influence of the markers is not visible. In the middle figure (b) the marker is visible and separated from the steel particle (bright area), leaving an air-gap between particle and marker/resin. Below the bubble structure of the resin is visible. The right figure (c) shows a steel particle without marker and has a very small surface roughness.

The elasto-hydrodynamic and piezo-viscous length scale were determined using Equations 2.14 and 2.15 and the particle and fluid properties of Tables 3.1 and 3.3 for $R = 5$ mm particles. As impact velocity, the settling velocity from Figure 2.1b is used. The data are listed in Table 3.1. Since $h_{pv} < h_{eh}$ piezo-viscous effects can be neglected. The roughness of steel particles approximately equals the elasto-hydrodynamic length scale, therefore steel particles might be considered to be smooth. This is not the case for delrin particles of which the size of the asperities is larger than the elasto-hydrodynamic length scale. Hence, delrin particles are considered to be rough.

A LaVision APX-RX 1 Mpx high-speed camera was used to record the motion of the falling particles. A frame-rate of 3000 frames per second was used to record the motion, except for the wet collisions with delrin spheres and an impact angle of 30.2 and 40.8 degrees for which a frame-rate of 1500 frames per second was used. Particles were illuminated from the back by a diffuse LED-panel to distinguish them from the background. To visualize the markers on the sphere, the opaque steel and delrin particles were illuminated from the front using a halogen light-source.

An alcohol thermometer, calibrated using a Julabo heat bath at several temperatures, was used to measure the temperature of the air/liquid inside the measurement tank before each measurement. Temperature differences from 19 to 23 degrees Celsius have been observed during the measurements, although at most times the temperature was around 21 degrees. The viscosity for water and air are therefore determined on the basis of a temperature of 21°C. The influence of the halogen light-source on the air/water temperature was observed to be negligible.

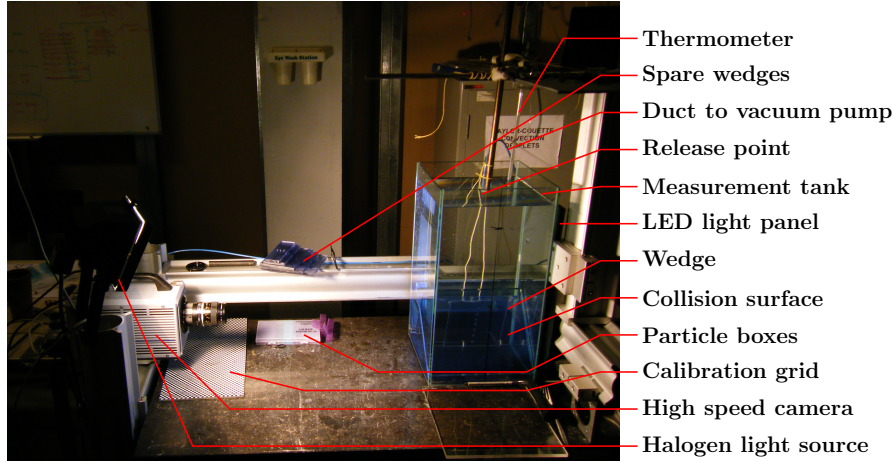


Figure 3.2: The experimental setup.

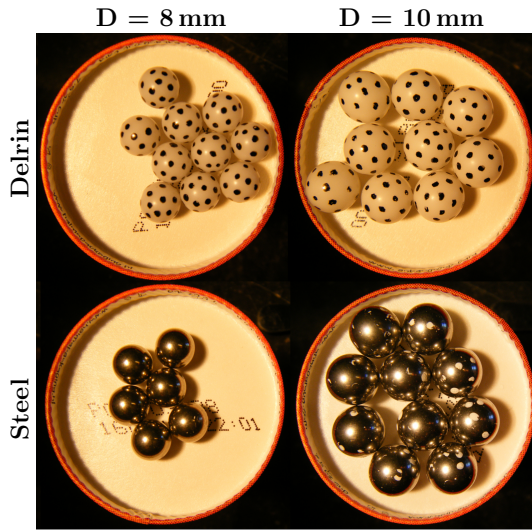
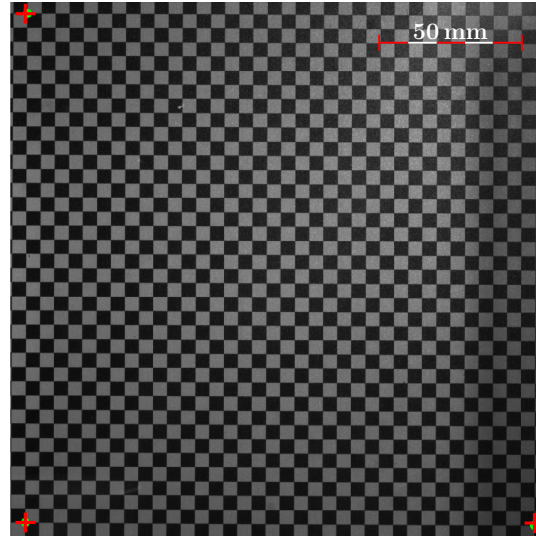


Figure 3.3: Delrin and stainless steel spheres with different diameters used within the experiment. Markers were manually applied using a permanent marker. More properties are listed in Table 3.1.

Figure 3.4: Calibration pattern made out of 5×5 mm squares. Green dots (●) and red crosses (+) depict the origin and extent of horizontal and vertical axes before and after the correction for the rotation of the camera, respectively.

Material	ρ [kg/m ³]	σ [μ m]	D [± 0.01 mm]	E [GPa]	ν	h_{eh} [μ m]	h_{pv} [μ m]
Stainless Steel	7200	0.7	8.00 & 10.00	189	0.30	0.6	0.12
Delrin (POM)	1420	3	8.00 & 10.00	3	0.35	1.1	0.06

Table 3.1: Specifications of the particles used in the experiment.

Material	l×w×h [mm]	ρ [kg/m ³]	σ [μ m]	E [GPa]	ν
Glass	250×250×10	2800	0.1	70	0.20

Table 3.2: Specifications of bouncing plate.

Material	ρ [kg/m ³]	μ_f [Pa·s]	$\hat{\eta}_f$ [Pa ⁻¹]
Air	1000	1.83×10^{-5}	-
Water	998	0.98×10^{-3}	10^{-9}

Table 3.3: Fluid specifications. The dynamic viscosity is determined for a fluid temperature of 21°C.

3.1.1 Calibration

The setup was calibrated using a checkerboard pattern, which was placed in the field of view of the camera covering the particle's plane-of-motion. Translation from pixel values to metric distances, as well as the correction for the rotation of the camera, was done by investigating the pixel values of the visible corners of the calibration grid as shown in Figure 3.4. Determination of the pixel values at origin and corners was done ten times and the average result was used to find the metric distances and rotation of the camera.

3.2 Data Analysis

The recorded video-frames were analyzed with the aid of Matlab and Python. Image processing, i.e. calibration and finding the position of both sphere and markers, was done using Matlab [MATLAB, 2014]. The data management and analysis was done with the Python [Van Rossum and de Boer, 1991; Oliphant, 2007; Millman and Aivazis, 2011] Scipy stack [Jones et al., 2001] and Numpy library [Van Der Walt et al., 2011]. Plotting was performed with the matplotlib library [Hunter, 2007]. Data transfer from Matlab to Python was done using intermediate data-files.

3.2.1 Position of Sphere & Markers

To find the position of the sphere and the markers placed thereon, the following procedure, as illustrated in Figure 3.5, was used:

1. Find particle outline, defined by its center position and radius, using Circular Hough Transform [Ballard, 1981] with `imfindcircles`.
2. Mask surroundings and in case of delrin spheres invert colors.
3. Mask pixels which have a value below the threshold value (thresholding).
4. Remove small (noise) and too large (reflections) areas.
5. Place marker at the centroid of each area.

The centroid position and radius found on the basis of the particle outline (1) are given with sub-pixel accuracy, and the radius was found to be in agreement

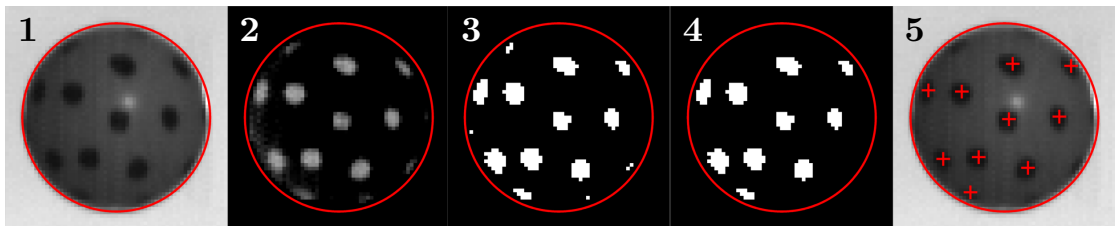


Figure 3.5: Procedure to find the outline (—) and markers (+) on a $R = 5$ mm delrin sphere.

with the measured size of the particle. Both threshold value (3) and criteria for the area size (4) are dependent on the particle type. Although the position of the markers (5) is given with sub-pixel accuracy, the error in the position of the markers proved to be of the order of one pixel due to changes in the shape of the markers between different frames. The procedure described above is applied to every recorded image/frame of each measurement.

3.2.2 Tracking the Particle Motion

The translational motion of the particle was obtained from the series of the sphere's center position in each frame. To find the rotation of the markers relative to the center of the sphere, Kabsch' algorithm [Kabsch, 1976, 1978] is used. This algorithm finds the optimal rotation matrix \mathbf{U} , which transforms the marker-coordinates from the initial (\mathbf{x}_n) to the rotated (\mathbf{y}_n) configuration. This is done by minimizing the following least-square error:

$$E = \sqrt{\frac{1}{N} \sum_{n=1}^N w_n (\mathbf{U}\mathbf{x}_n - \mathbf{y}_n)^2}, \quad (3.1)$$

where \mathbf{x}_n and \mathbf{y}_n , $n \in \{1, \dots, N\}$ are the coordinates of the correlated markers on the sphere, $w_n = 1$ the weight corresponding to each pair \mathbf{x}_n , \mathbf{y}_n and E the residual quantity which has to be minimized.

From the rotation matrix, the Euler-Cardan angles θ , ψ and φ around respectively x , y and z axis are extracted, where $\mathbf{U} = \mathbf{U}_z(\varphi) \cdot \mathbf{U}_y(\psi) \cdot \mathbf{U}_x(\theta)$.³ Appendix B gives an elaborate discussion about the Kabsch algorithm and its sensitivity to measurement uncertainties in the position of the markers.

The correlation between the markers, mandatory for Kabsch' algorithm, is done using nearest-neighbor interpolation between the points in the reference and rotated frame. A restriction of the correlation distance by a maximum absolute displacement of $R\pi/16$ and radial displacement of $R/8$ was found to be appropriate.⁴ Injective mapping of points satisfying the constraints is ensured by choosing the nearest neighbor if two points in the initial frame are mapped to the same one in the rotated frame. To reduce the signal to noise ratio in the resulting angles both the correlation and kabsch algorithm were applied to frame n and $n + n_{\text{skip}}$, with $n_{\text{skip}} = 5$. For $n_{\text{skip}} < 3$ and $n_{\text{skip}} > 8$ deviations in some of the resulting angles were observed. With the uncertainty of 1 pixel (~ 0.18 mm) in the position of the marker the resulting uncertainty of the angles was in agreement with the results from Appendix B.

Figure 3.6a shows the trajectory followed by a $R = 5$ mm delrin sphere colliding on a surface with an incidence angle of $\xi_{\text{in}} = 14.7$ degrees. The instant of contact

³The non-commutative nature of the rotation matrix requires a definition of order in which the rotations are performed. As convention we take the rotations subsequently around x , y and z axis.

⁴These values are chosen by investigating the erroneous correlated markers, and looking for restrictions removing the wrongly correlated markers without influencing the markers which were properly correlated.

was found from the minimum normal distance of the particle to the plate. To track the particle's motion prior to and just after the collision the data was fitted using piecewise continuous polynomial functions. The translational motion was determined using a piecewise second-order polynomial function from 50 points before to 50 points after the collision point, with the discontinuity at the collision point. The velocity and acceleration were obtained from its temporal derivatives. This procedure is illustrated in Figures 3.6c and 3.6d. The angular velocity of particles is found using by piecewise smoothening of the signal from the Kabsch algorithm and then fitting a horizontal line to the points before the collision and the points after the collision. This procedure is illustrated in Figure 3.6b.

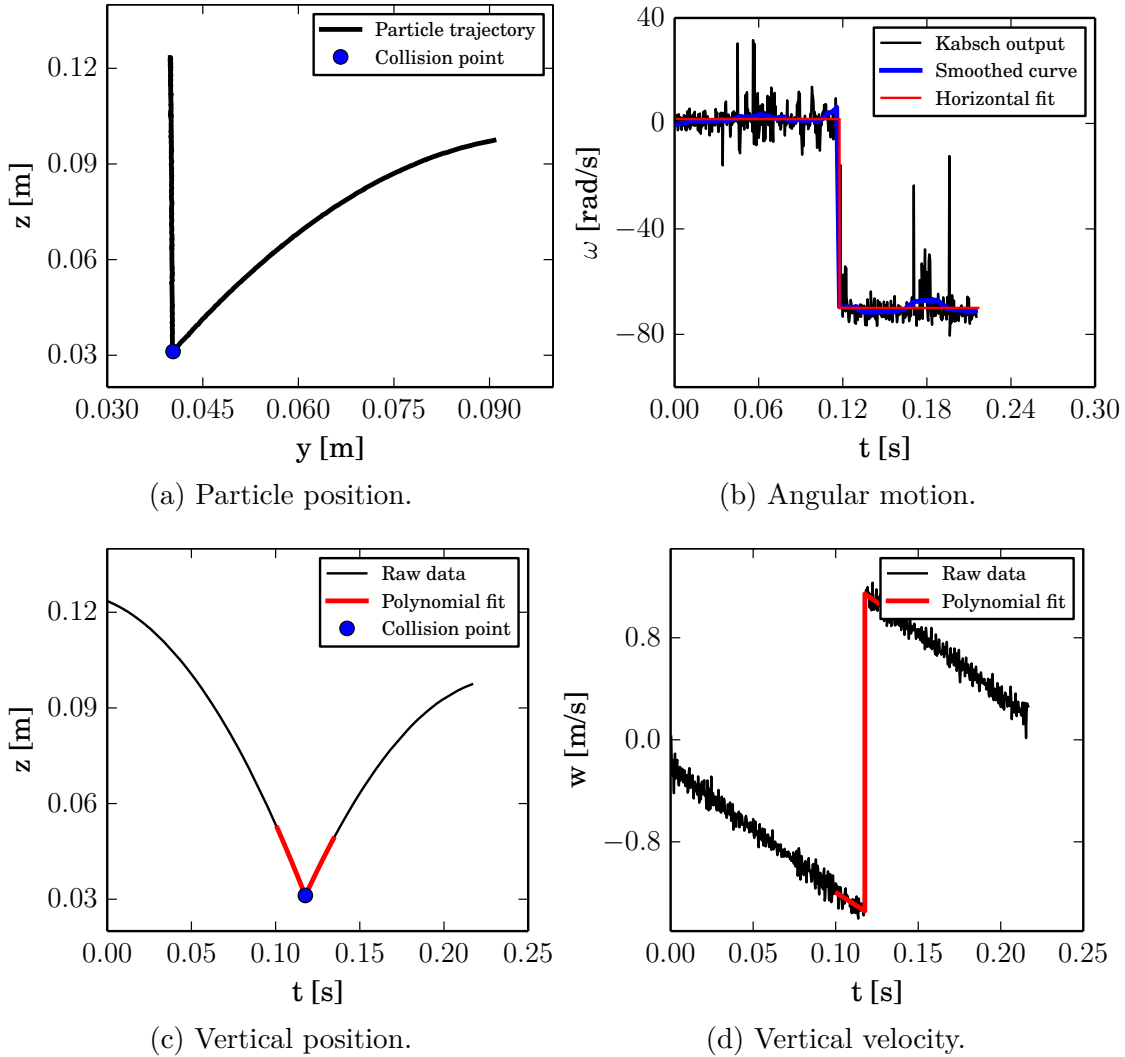


Figure 3.6: Linear motion and rotation of a $R = 5$ mm delrin particle falling on a plane with incidence angle $\xi_{\text{in}} = 14.7$ degrees. Figure (a) shows the particle position. Figure (b) shows the rotation obtained by application of the Kabsch algorithm. The large erroneous results in the original output are the result of mis-correlation between markers or the detection of markers which in reality do not exist. Since the number of these errors is small they vanish during the smoothing process. In figure (c) the vertical position of the particle in time is shown. From the 2nd order piecewise polynomial fit near the bouncing point the velocity component w in the z -direction, shown in figure (d) is found just before and after impact. The raw velocity data are obtained by taking the temporal derivative of the raw vertical position using second order accurate central differences. The polynomial fit in the vertical velocity is the temporal derivative of the polynomial fit from figure (c). A similar procedure is followed for the motion in the horizontal (y) direction.

4 Results

This chapter is dedicated to the experimental results and compares them with the presented model and other datasets from literature. The results will be presented in a manner following the order of the theoretical analysis of Chapter 2. The results for the separate parameters of Walton's three parameter model are plotted against the incidence angle in Section 4.1. These data are combined in a master-curve in which the normalized incidence angle is set out against the normalized rebound angle. Section 4.2 shows the results for the wet collision. Finally, it is shown that the effective normal coefficient of restitution is dependent on the Stokes impact number based on the normal impact velocity.

4.1 Dry collisions

Measurements were obtained for collisions of steel and delrin spheres with a radius of 5mm at 8 different impact angles ξ_{in} . For each material two particles were used to take 5 measurements at the different impact angles. Particles were released from approximately 10 cm above the surface, resulting in an impact velocity of 1 ms^{-1} as shown in Figure 2.1b. The effective angles of incidence and rebound are computed using Equation 2.5 and plotted against each other in Figure 4.1. From this figure it is observed that the results corresponding to the 5 lowest incidence angles belong to the stick regime, whereas the 3 highest incidence angles are in the slip regime of Walton's model.

The three parameters describing the collision, according to Walton's model (2.10), are plotted in Figure 4.2. The Coulomb coefficient of sliding friction is obtained by fitting a horizontal line to the results belonging to the slip regime. The resulting coefficient of sliding friction is given by $\mu_f = 0.099 \pm 0.003$ for steel and $\mu_f = 0.114 \pm 0.007$ for delrin particles. The value for the collision of the steel particle is in line with the result of Joseph and Hunt [2004], who obtained $\mu_c = 0.11 \pm 0.003$ for steel spheres impacting on a zerodur surface.

The tangential coefficient of restitution is obtained by fitting a horizontal line to the results corresponding to the stick regime. This results in $e_t = 0.18 \pm 0.16$ for steel and $e_t = 0.40 \pm 0.05$ for delrin particles. The large uncertainty in the tangential coefficient of restitution for steel particles is due to the large spread in the data for the different incident angles. The value for the collision of the steel particle is lower than the $e_{t,d} = 0.34 \pm 0.07$ found by Joseph and Hunt [2004] for steel spheres impacting on a zerodur surface.

The normal coefficient of restitution for steel particles is given by $e_n = 0.885 \pm 0.007$ and $e_n = 0.951 \pm 0.008$ for delrin particles. The value for the collision of

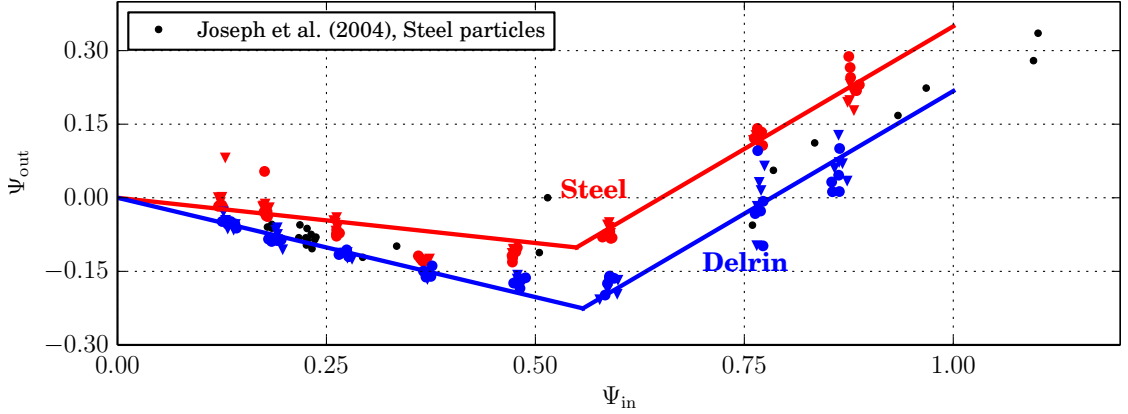
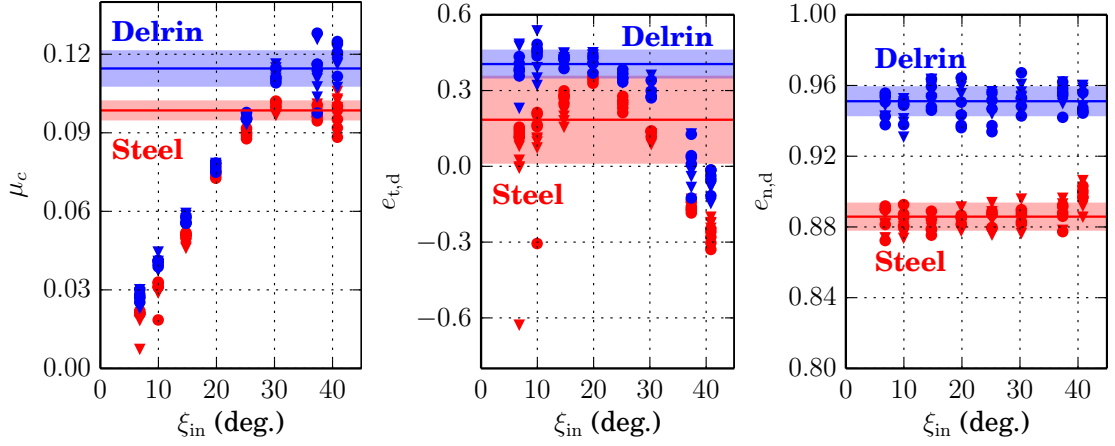


Figure 4.1: Dry collision results fitted with Walton’s collision model. Results are shown for $R = 5\text{mm}$ delrin and steel particles.



(a) Coulomb coefficient of sliding friction. (b) Tangential coefficient of restitution. (c) Normal coefficient of restitution.

Figure 4.2: Parameters involved in Walton’s collision model as function of the incidence angle for dry collisions. Each marker corresponds to a single measurement. Similar marker types indicate that the measurement is carried out with the same particle. The horizontal fit of the data for μ_c and $e_{t,d}$ was performed on the results belonging to the slip and stick regime, respectively.

the steel particle is in line with the result of Joseph et al. [2001], who obtained $e_{n,d} = 0.88 \pm 0.07$ for steel spheres colliding on a glass surface, but low compared to the $e_{n,d} = 0.97 \pm 0.01$ found by Gondret et al. [2002] and the $e_{n,d} = 0.97 \pm 0.01$ of Joseph and Hunt [2004]. Energy dissipation due to inelastic deformation of the wedge setup might be responsible for this lower value for steel particles. The normal coefficient of restitution for the delrin spheres is in line with the $e_{n,d} = 0.95 \pm 0.02$ found by Gondret et al. [2002]. The lower impact force on the plane may for this case not lead to deformations in the wedge setup.

Based on the collision parameters found from Figure 4.2 the lines corresponding to Walton’s collision model (2.10) are plotted in Figure 4.1. Although the results for steel particles are qualitatively well in agreement with the data from Joseph and Hunt [2004], the lower value for the normal and tangential coefficient of restitution result in a different line in Walton’s model.

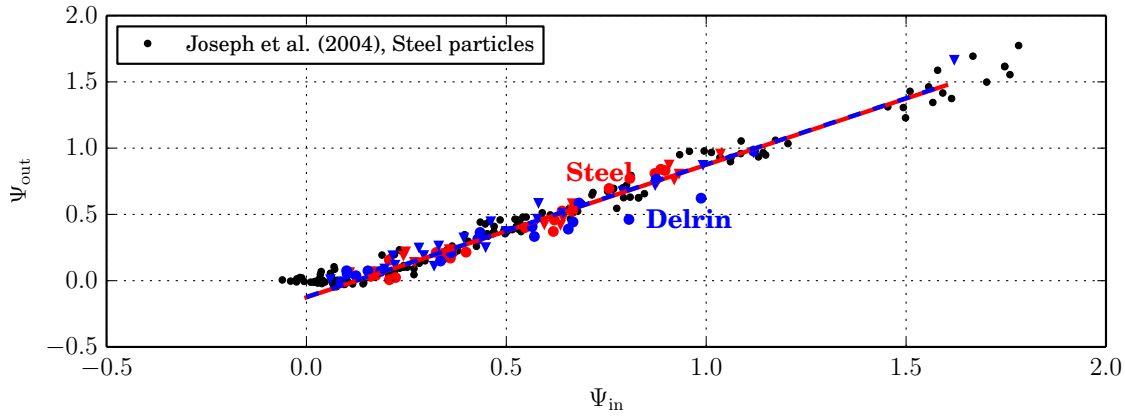
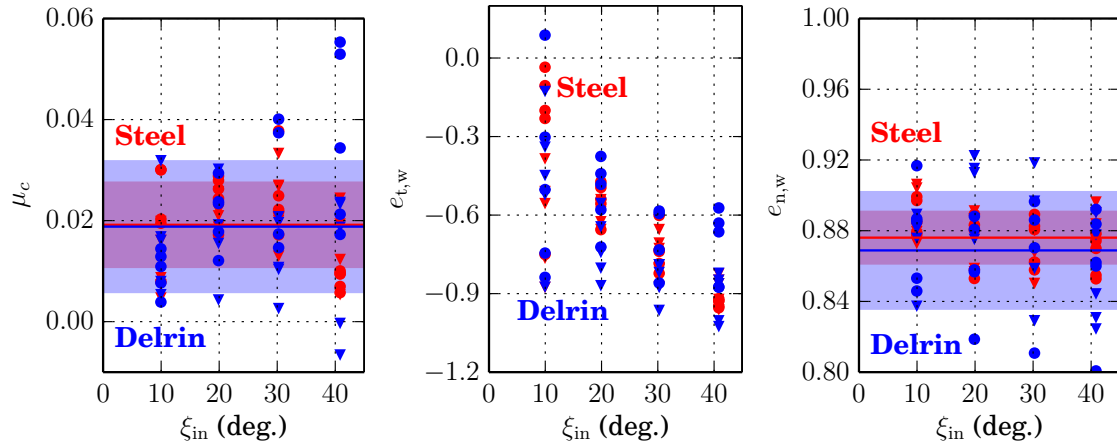


Figure 4.3: Wet collision results compared to the collision model of Walton. Results are shown for $R = 5\text{mm}$ delrin and steel particles. The absence of a stick regime in combination with a very small value for the coefficient of sliding friction implies that both the steel and delrin particles can be considered to be smooth.



(a) Coulomb coefficient of sliding friction. (b) Tangential coefficient of restitution. (c) Normal coefficient of restitution.

Figure 4.4: Parameters involved in Walton's collision model as function of the incidence angle for wet collisions. Each marker corresponds to a single measurement. Similar marker types indicate that the measurement is carried out with the same particle. The horizontal fit of the data for μ_c belonging to the slip regime. Due to the absence of results belonging to the stick regime a fit to the data of $e_{t,w}$ was omitted.

4.2 Wet collisions

Measurements were obtained for collisions of steel and delrin spheres with a radius of 5mm at 8 different impact angles ξ_{in} . For each material two particles were used to take 5 measurements at the different impact angles. Particles were released from the top of the aquarium and (almost) reached their terminal settling velocity before impact. From Figure 2.1 one observes that the impact velocity of the steel particles is approximately 1.4ms^{-1} and 0.3ms^{-1} for the delrin spheres. The effective angles of incidence and rebound are computed using Equation 2.5 and

plotted against each other in Figure 4.3. From this figure it is observed that the results corresponding all incidence angels belong to the slip regime of Walton's collision model.

The three parameters describing the collision, according to Walton's model (2.10), are plotted in Figure 4.4. The Coulomb coefficient of sliding friction is obtained by fitting a horizontal line to the results belonging to the slip regime, in this case all results. The resulting coefficient of sliding friction is given by $\mu_f = 0.018 \pm 0.003$ for steel and $\mu_f = 0.018 \pm 0.012$ for delrin particles, and thereby both an order of magnitude lower than the coefficient of sliding friction of the dry case.

The results for the tangential coefficient of restitution decrease to a value of -1, which indicates a full sliding collision. The spread in the data increases for lower incidence angles. Both observations are in line with Joseph and Hunt [2004].

The normal coefficient of restitution for steel particles is given by $e_n = 0.87 \pm 0.01$ and $e_n = 0.86 \pm 0.03$ for delrin particles. The value for the steel particles is, just as in the dry case, lower than result of Gondret et al. [2002], whereas the results for the delrin particles agree. Energy losses due to inelastic deformation in the wedge setup might be responsible for this lower value, since the impact velocity is of the same order as for the dry collisions.

Based on the results from Figure 4.4, the lines corresponding to Walton's collision model (2.10) are plotted in Figure 4.3. Since the stick regime is not present in the dataset, due to the small coefficient of sliding friction, only the function corresponding to the slip regime is shown. Therefore the particle does not interact with the wall through the roughness elements. Hence, both steel and delrin particles may considered to be smooth. This is not in line with the result from in Section 3.1, in which was found that the delrin particles were rough, since the surface roughness was larger than the elasto-hydrodynamic length scale, i.e. $\sigma > h_{eh}$. The smooth behavior might be caused by the deformation of the roughness elements upon impact on the very smooth collision plate. For steel spheres, for which $\sigma \approx h_{eh}$ the smooth behavior confirms the cautious conclusion of Section 3.1 stating that the steel spheres might considered to be smooth.

4.2.1 Coefficient of restitution

Figure 4.5 shows the effective normal coefficient of restitution, i.e. the ratio between the normal wet and the normal dry coefficient of restitution, as function of the Stokes number based on the normal impact velocity. Each data-point resembles the average of 5 measurements with corresponding standard deviation. Measurements were obtained for collisions of steel and delrin spheres with a radius of 4 and 5 mm. The results from collisions following after the first impact are connected to the data-point corresponding to the previous impact. Since the impact Stokes number decreases with the number of collisions, due to the inelasticity of the collision, the most right point correspond to the first impact.

The results for both steel and delrin particles falls within the scatter of the data from Joseph and Hunt [2004] and the empirical fit (2.13) from Legendre et al.

[2006], which lies within the uncertainty region of nearly each measurement. Hence, our results are in line with previous experiments stating that the normal coefficient of restitution as function of the normal Stokes impact is similar to a normal collision with the same velocity.

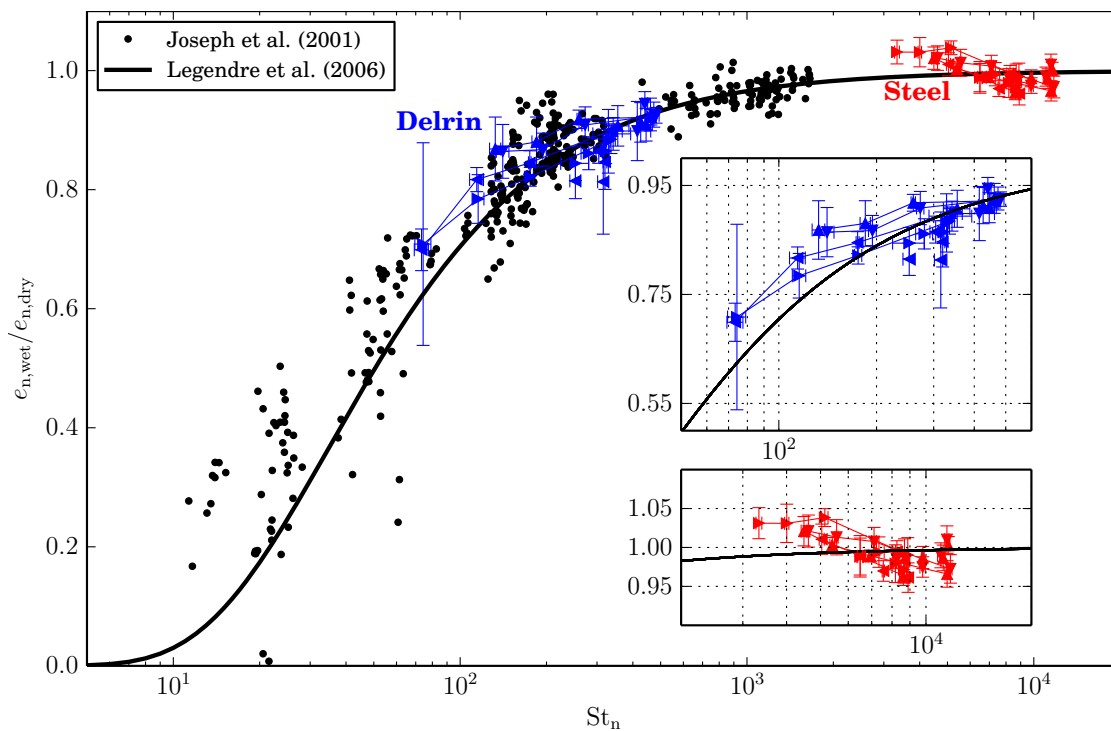


Figure 4.5: Effective normal coefficient of restitution for steel and delrin spheres with diameters $R = 4\text{mm}$ and $R = 5\text{mm}$. The line indicates empirical fit (2.13) from Legendre. et al. [Legendre et al., 2006]. If present, data from the second bounce are connected with a line to the result of the initial collision, and the data from the third to the second... and so forth. Insets show enlarged the results of the present work.

5 Conclusions

This chapter concludes the findings of the previous chapters and presents recommendations for further research.

The objective of the present study was to investigate the hydrodynamic interaction of a spherical particle colliding obliquely onto a planar surface. We presented an experimental dataset with results of steel and delrin particles colliding onto an inclined glass plate. The macroscopic collision model of Walton [1993] was used to describe the results. This model depends on three parameters: the coefficient of sliding friction μ_f , the tangential coefficient of restitution e_t and the normal coefficient of restitution e_n .

In order to find both the translation and the rotation of a spherical particle, markers were applied particle's surface. The particle was released with negligible initial rotation from a vacuum tube, and the motion of the particle colliding with the plate was recorded using a high speed camera. The tracking of both sphere and markers was very sensitive to the illumination of both sphere and marker. With the aid of Kabsch' algorithm and the positions of the markers on the sphere the rotation of the particle was found. The rotational results and their uncertainty were in agreement with the uncertainty arising from the Kabsch algorithm which was investigated both analytically and numerically.

From the wet collisions it became clear that both the steel and delrin spheres could considered to be smooth. As a consequence, and in agreement with earlier studies, the coefficient of sliding friction dropped almost one order of magnitude compared to the dry collisions. Finally we observed, in agreement with Joseph and Hunt [2004], that the normal coefficient of restitution is independent to the obliqueness of the collision surface when only the normal component of the collision is taken into account.

The agreement of the data with the results from literature indicates that the presented setup is suitable to investigate oblique particle-wall collisions. However the detection of the particles and marker proved to be a challenge, with the result that the collisions of glass particles could not be measured. Due to the difficult detection of the markers and the correlation of the markers between frames, no information about the rotation of the $R = 4$ mm spheres was obtained. It is therefore recommended that for further experiments the simple marker detection algorithm, based on thresholding, is replaced by a more stable detection method.

The results presented in this thesis, add to the few data present in literature by using a different setup. Since the results for both wet and dry collisions were in

agreement with the data from literature, this work may be used as validation for the modeling of particle laden flows.

With the measurement technique presented in this thesis simple particle-particle interactions can be studied. An example is the drafting-kissing-tumbling phenomenon in which a particle is accelerated in the wake of another particle and finally collides with this particle. Another possibility is to study the motion of a particle over a surface. Although the normal contact force, and thereby the tangential contact force, will in general be lower, still a coefficient of sliding friction is required to estimate whether the particle will roll or slide over the surface. A further study could investigate the drafting-kissing-tumbling of particles moving over a surface. Since both particle-particle and particle-wall interactions are present, such an experiment will provide a valuable dataset to validate the four-way coupling of numerical simulations.

A Particle Surface Roughness

This chapter adds the detailed information about the determination of the surface roughness of the particles collision surface. In the case of the particles both an optical and scanning technique has been used to investigate the surface roughness and the influence of the added markers thereon. The surface roughness of the plate is only investigated using the scanning technique. Section A.1 discusses the measurement techniques. The results are presented in Section A.2.

A.1 Method

A.1.1 Optical

In order to optically study the particle's surface roughness, the particles were embedded in a clear acrylic cold mounting resin ClaroCit and sawn into halves. For ease only a large marker was placed in the cutting line. The sawn surface was polished in five consecutive steps, starting with coarse grinding paper and finishing with a polishing fluid, till a roughness of less than $2.5\ \mu\text{m}$ was achieved. Figure A.1 shows the embedded, sawn and polished particles. This procedure was applied to two $R = 5\ \text{mm}$ steel particles and two $R = 6\ \text{mm}$ delrin particles.⁵

Subsequently the particles were placed under an optical microscope and the edge profile of the embedded particle was visually investigated.

A.1.2 Stylus

Stylus measurements have been performed using a Tencor 500 profiler on both particles and collision plate. The sample was placed on a moving table and scanned by a needle with a radius of $12.5\ \mu\text{m}$ over a length of $4\ \text{mm}$ with a speed of $0.02\ \text{mm/s}$ and a stylus force of $10\ \mu\text{g}$. The maximal vertical resolution of the profiler was given to be $0.1\ \text{nm}$.

The raw scan data of the needle height and scan-length were exported in a datafile. To remove macroscopic movement of the needle due to the curvature of the particles and a non-horizontal mounting of the table, the data were fitted with and subtracted by a moving average. The particle surface roughness σ is determined from the 95% confidence level of the size of the asperities.

⁵Since the low amount of delrin particles present for the experiment it was decided to cut the particles of the size that was not used in the experiment. The surface properties of all delrin particles were assumed to be equal.

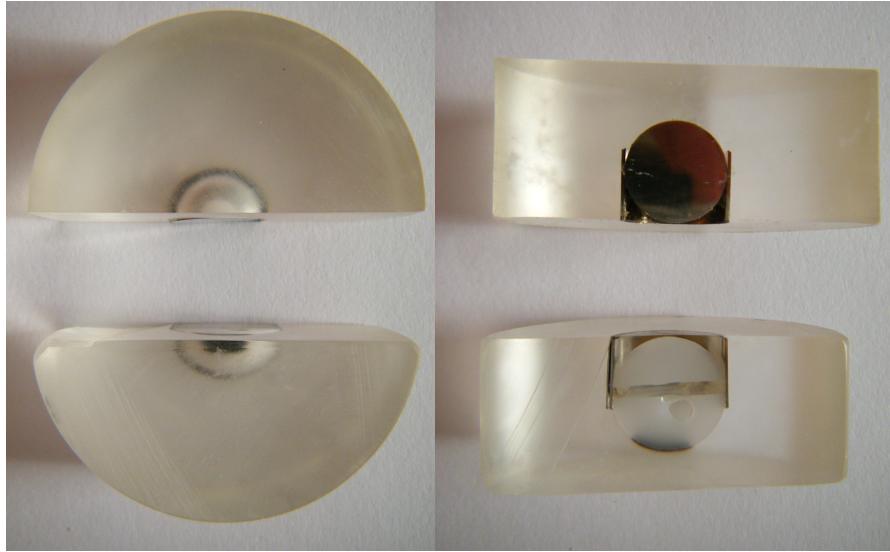
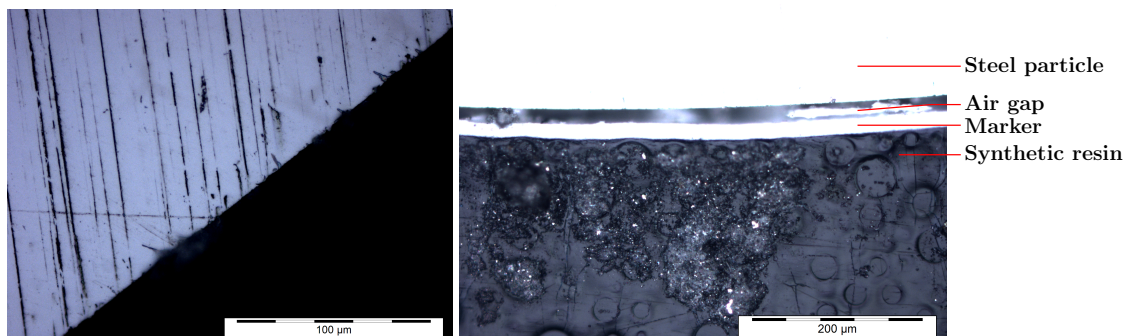


Figure A.1: Side and top view of steel (upper figures) and delrin (lower figures) particles embedded in a synthetic resin. The side view clearly shows the white and black marker present on the steel and delrin sphere, respectively. In the top view of the delrin particle a cutting line from a previous unsuccessful cut is visible. The clear visibility of the black marker is due to the dissolution of the marker in the resin. For delrin particles the splitting of the particles revealed the presence of a small air bubble within each particle.



(a) Without marker.

(b) With marker.

Figure A.2: Edge of $R = 5$ mm steel particles visualized using a microscope. The left figure (a) shows region without marker. The scratches on the particle originate from the polishing process and have a separation of at least $2.5 \mu\text{m}$. The right figure (b) shows a region with a marker. The marker is separated from the particle by the resin leaving an air-gap between particle and marker.

A.2 Results

A.2.1 Steel Particles

Figures A.2a and A.3 show the surface profile of a $R = 5$ mm steel particle without marker. From the stylus measurement the surface roughness is estimated to be $0.7 \mu\text{m}$. Figures A.2b and A.4 show the surface profile of a similar particle with marker. In both the optical as stylus measurement the marker is clearly visible. The thickness of the marker is estimated to be approximately $20 \mu\text{m}$. A collision on the marker may therefore result in anomalous results. As explained in Chapter 3 the markers are therefore only applied to the fronal area of the sphere.

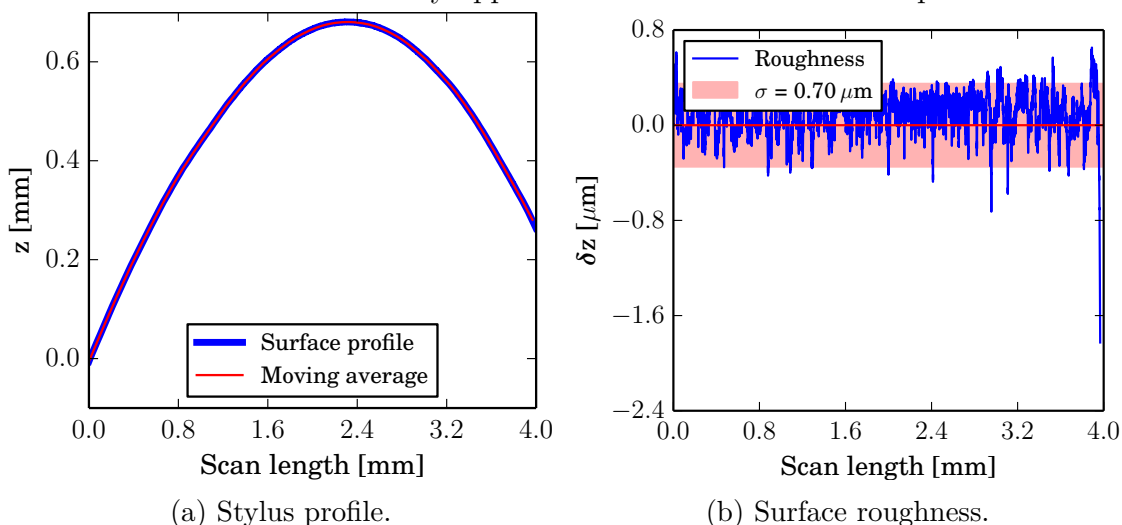


Figure A.3: Stylus line-scan of the surface of a steel particle without scanning over a marker. Figure (a) shows the surface profile and the corresponding moving average. In figure (b) the surface profile is subtracted by the moving average. The surface roughness is estimated to be $0.7 \mu\text{m}$.

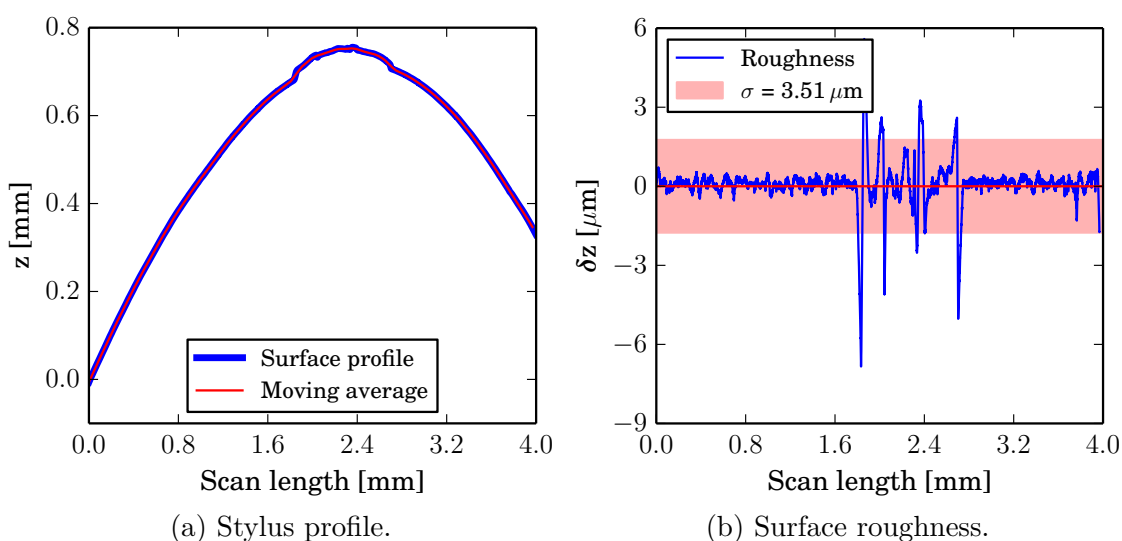


Figure A.4: Stylus line-scan of the surface of a $R = 5$ mm steel particle over a marker. Figure (a) shows the surface profile and the corresponding moving average. The marker is clearly visible on top of the particle and has a size of approximately $20 \mu\text{m}$. In figure (b) the surface profile is subtracted by the moving average, thereby losing the information of the marker's size.

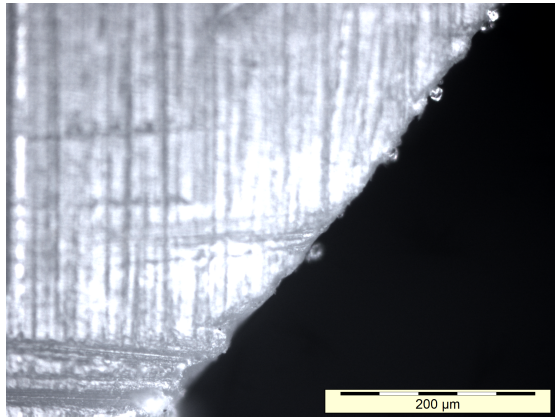


Figure A.5: Edge of $R = 6$ mm delrin particle visualized using a microscope. The scratches on the particle originate from the polishing process and have a separation of at least $2.5 \mu\text{m}$. The marker on the particle which was clearly visible in Figure A.1 was not observed under the microscope.

A.2.2 Delrin Particles

Figure A.5 shows the edge of a $R = 6$ mm delrin particle. On the particle's surface some roughness elements are visible with a size of approximately $10 \mu\text{m}$. The results of the stylus measurements, shown in Figure A.6 also shows an asperity with a size of $10 \mu\text{m}$, although this is an indentation instead of roughness element raised from the surface. Like in the optical figure, the marker is also not observed in the stylus profile as shown in Figure A.7. The surface roughness of $2.3 \mu\text{m}$ is significantly smaller than the $4.03 \mu\text{m}$ found from Figure A.6 due to the absence of large roughness elements. This leads to the conclusion that the particle's roughness is approximately $3 \mu\text{m}$, and some sparse larger roughness elements are present on the particle's surface. Furthermore it is observed the markers do not enhance the surface roughness of the delrin particles.

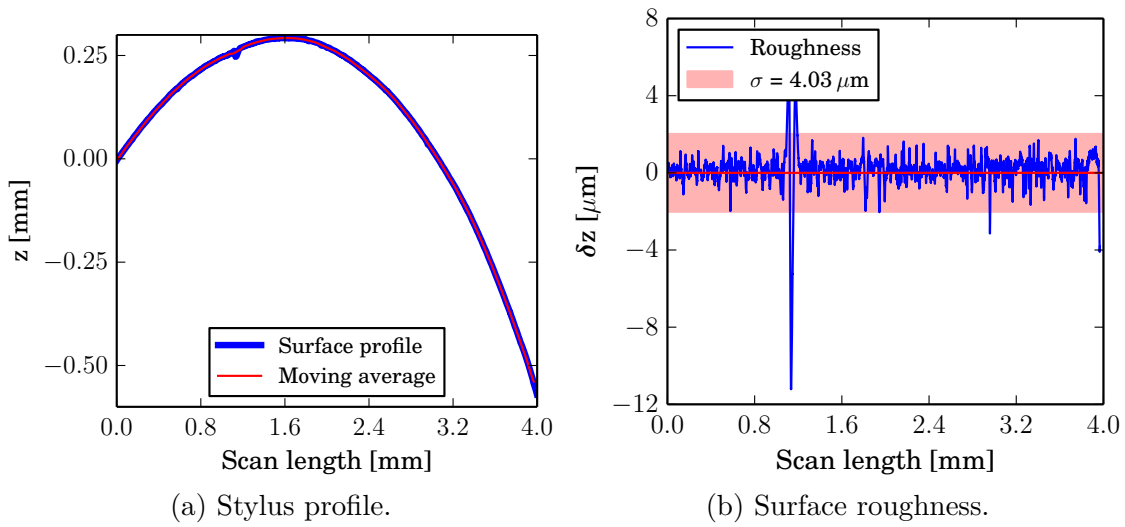


Figure A.6: Stylus line-scan of the surface of a $R = 5$ mm delrin particle without scanning a marker. Figure (a) shows the surface profile and the corresponding moving average. The surface has a small dimple at 1.1 mm with a size of approximately $10 \mu\text{m}$. The surface roughness is estimated to be $4.0 \mu\text{m}$.

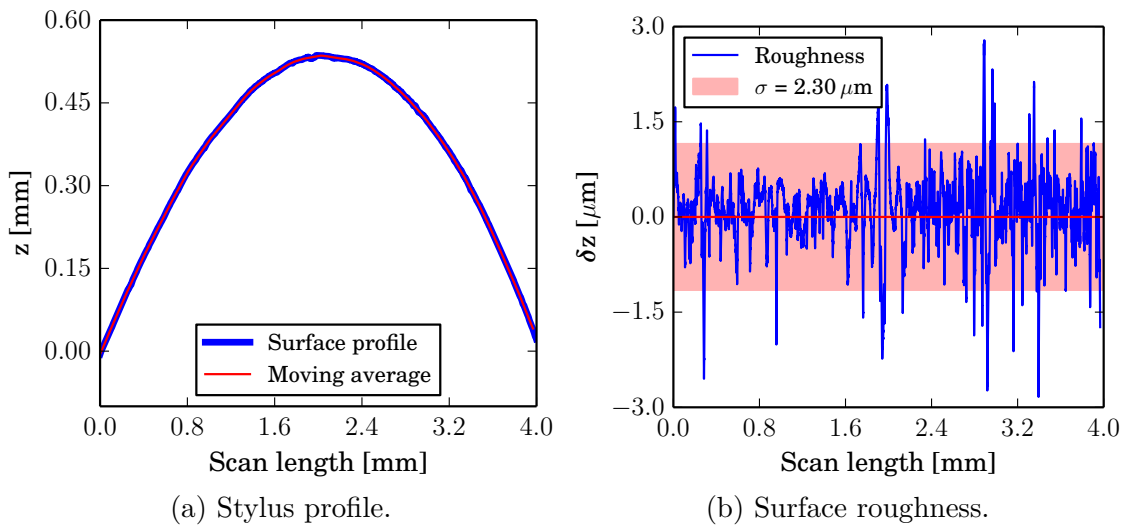


Figure A.7: Stylus line-scan of the surface of a $R = 5$ mm delrin particle over a marker. Figure (a) shows the surface profile and the corresponding moving average. The marker does not enhance the particle's surface profile. In figure (b) the surface profile is subtracted by the moving average. The surface roughness is estimated to be $2.3 \mu\text{m}$.

A.2.3 Glass Surface

Figure A.8 shows the stylus profile of the glass collision surface, which proves to be very smooth with a roughness of $0.09 \mu\text{m}$. The enhancement of the surface topology due to the few scratches visible on the plate is shown in Figure A.9. The depth of the scratch is observed to be $1 \mu\text{m}$.

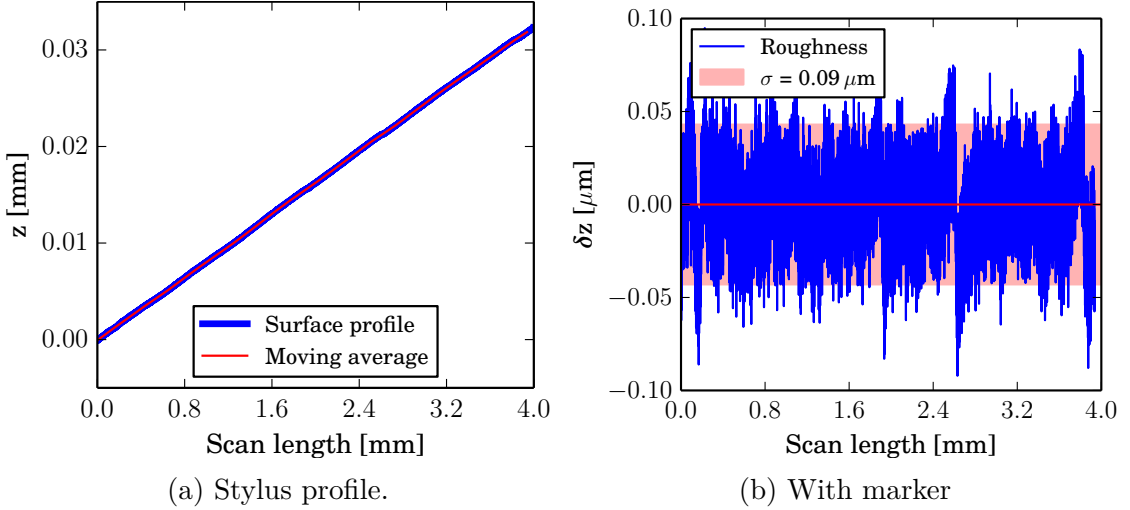


Figure A.8: Stylus line-scan of the surface of the glass collision plate. Figure (a) shows the surface profile and the corresponding moving average. In figure (b) the surface profile is subtracted by the moving average. The surface roughness is estimated to be $0.09 \mu\text{m}$.

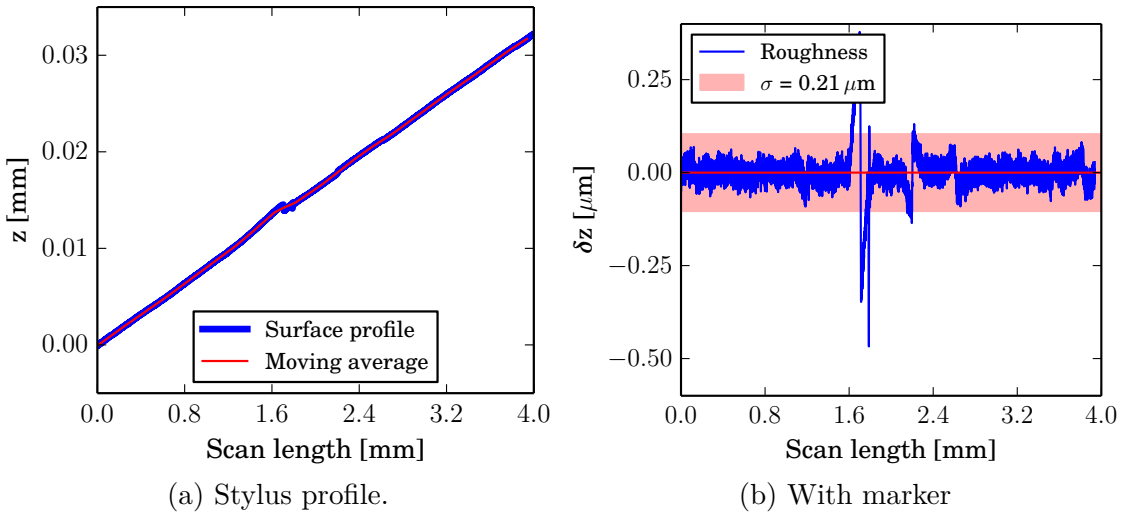


Figure A.9: Stylus line-scan crossing a visible scratch on the surface of the glass collision plate. Figure (a) shows the surface profile and the corresponding moving average. Although the scratch was visible to the naked eye the depth is approximately $1 \mu\text{m}$. In figure (b) the surface profile is subtracted by the moving average, thereby losing the information of the exact depth of the scratch.

B Kabsch Algorithm

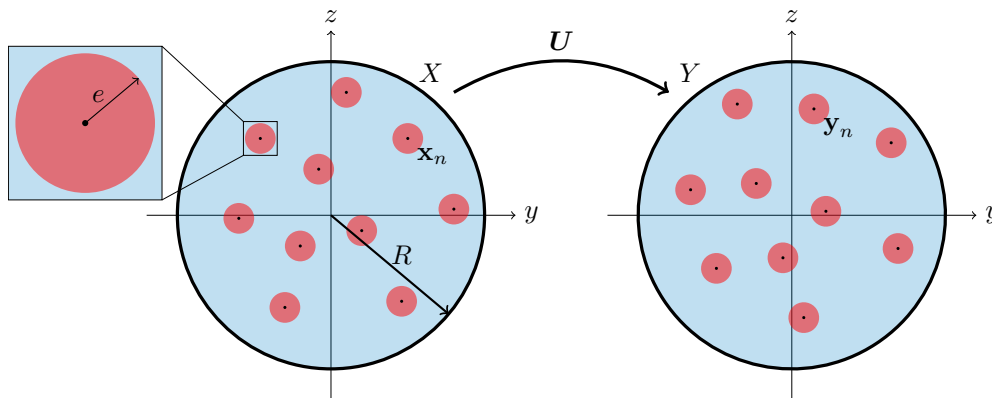
Abstract

The Kabsch-algorithm [Kabsch, 1976, 1978] has been designed to find the optimal rotation matrix between two sets of points by minimization of the root mean square of the separation between the points. The algorithm was originally intended to compare molecular configurations in chemistry, but can also be used to find the rotation of a particle [Klein et al., 2013]. However this method is found to be very sensitive to the measurement uncertainties in the position of the markers applied to the sphere, resulting in an inaccurate result for the rotation of the particle.

In this appendix we will investigate, both analytically and numerically, the influence of the measurement uncertainty of the position of the markers on the measured angles. An analytical estimate of the error in the measured angle is obtained from linearization of the rotation matrix. To check the analytical estimate, the error was also computed numerically in which the measurement uncertainties were represented by random perturbations to the points on the sphere.

Subsequently the effect of averaging over multiple experiments, which is assumed to reduce the measurement error, is investigated. The influence of the angle of rotation is also investigated, since small deviations in the position of the sphere may have more influence on small rotations than on large ones. Furthermore the influence of the radius of the sphere and the amount of markers applied to the sphere is treated.

Graphical Abstract



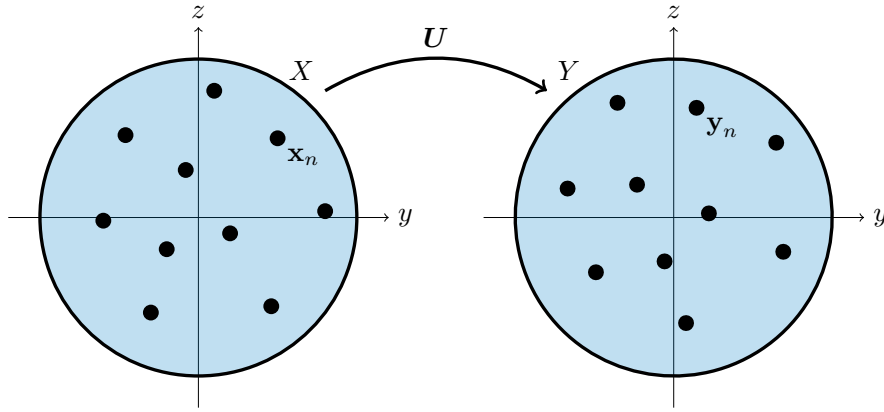


Figure B.1: Schematic representing the use of the Kabsch algorithm. An optimal rotation matrix \mathbf{U} has to be found which maps the markers (black) of the reference configuration (\mathbf{x}_n stored in X) the best to those in the rotated configuration (\mathbf{y}_n stored in Y).

B.1 Theory and Propagation of Uncertainties

The Kabsch algorithm [Kabsch, 1976, 1978] was developed to find molecular rotations in chemistry, however this method can also be used to study the rotation of rigid objects and especially spheres [Klein et al., 2013]. When N markers are applied on a sphere, all points will have the same center of rotation, namely the center of the sphere. The Kabsch algorithm finds the optimal rotation matrix which transforms the markers from the initial to the rotated configuration. From this matrix the Euler-Cardan angles describing the rotation of the sphere can be found.

B.1.1 Theory

Consider two coordinate sets X and Y of N paired points, as shown in Figure B.1, for which we have to find the unitary matrix \mathbf{U} which maps X the best to Y . This leads to the following minimization problem

$$E = \sqrt{\frac{1}{N} \sum_{n=1}^N w_n (\mathbf{U}\mathbf{x}_n - \mathbf{y}_n)^2}, \quad (\text{B.1})$$

in which \mathbf{x}_n and \mathbf{y}_n , $n \in \{1, \dots, N\}$ are the coordinates of the corresponding markers on the sphere⁶, w_n the weight corresponding to each pair \mathbf{x}_n , \mathbf{y}_n and E the residual quantity which has to be minimized. This problem can be rewritten

⁶Since all coordinates \mathbf{x}_n , \mathbf{y}_n are lying on a sphere all coordinates have the same length R . Therefore points lying closer/further from the origin do not give a lower/higher contribution to E . Therefore the resulting angles are not almost entirely determined by the displacements of the points located far from the origin.

as

$$NE^2 = \sum_{n=1}^N w_n [(\mathbf{U}\mathbf{x}_n)^2 + \mathbf{y}_n^2 - 2\mathbf{U}\mathbf{x}_n\mathbf{y}_n]. \quad (\text{B.2})$$

Minimizing the left-hand side is equivalent to maximizing the last and negative term on the right hand side. If the N markers \mathbf{x}_n and \mathbf{y}_n are stored as $3 \times N$ matrices in X respectively Y , the following quantity has to be maximized

$$\sum_{n=1}^N w_n \mathbf{U} X_n Y_n = \text{Tr}(Y^T \mathbf{U} \hat{X}) = \text{Tr}((\hat{X} Y^T) \mathbf{U}), \quad (\text{B.3})$$

with $\hat{X}_{mn} = w_n X_{mn}$, $m \in \{1, 2, 3\}$, $n \in \{1, \dots, N\}$. Rewriting $\hat{X} Y^T$ using its singular value decomposition (SVD) as $\hat{X} Y^T = V S W^T$, in which V and W^T are orthogonal matrices of the right eigenvectors of $\hat{X} Y^T$ and S a diagonal matrix containing its eigenvalues ($s_1 \geq s_2 \geq s_3$), this equation can be rewritten as

$$\text{Tr}((\hat{X} Y^T) \mathbf{U}) = \text{Tr}(V S W^T \mathbf{U}) = \text{Tr}(S W^T \mathbf{U} V) = \sum_{i=1}^3 s_i T_{ii}, \quad (\text{B.4})$$

where we made use of the commutative properties of the trace operator. The 3×3 orthogonal matrix T is given by $T = W^T \mathbf{U} V$. Orthogonality of T implies all its elements are smaller than 1, so in order to maximize equation B.4, T has to be the identity matrix I .

Assuming a right handed coordinate system, we must have $\det(\mathbf{U}) = 1$. This holds for $\det(\hat{X} Y^T) > 0$ but when $\det(\hat{X} Y^T) < 0$ we have $\det(\mathbf{U}) = -1$. In the latter case, the second largest value of equation B.4 has to be used. Since $s_1 \geq s_2 \geq s_3$ this value is found when $T_{33} = -1$. The optimal rotation matrix is therefore given by

$$\mathbf{U} = W \begin{bmatrix} 1 & 0 & 0 \\ 0 & 1 & 0 \\ 0 & 0 & d \end{bmatrix} V^T \quad d = \text{sign}(\det(\hat{X} Y^T)). \quad (\text{B.5})$$

Assuming that the rotation matrix \mathbf{U} is build up as follows from the rotation matrices $\mathbf{U}_x(\theta)$, $\mathbf{U}_y(\psi)$ and $\mathbf{U}_z(\varphi)$

$$\mathbf{U} = \mathbf{U}_z(\varphi) \cdot \mathbf{U}_y(\psi) \cdot \mathbf{U}_x(\theta), \quad (\text{B.6})$$

the Euler-Cardan angles of rotation around respectively x -, y - and z -axis θ , ψ and φ are given by

$$\theta = \tan^{-1} \left(\frac{\mathbf{U}_{32}}{\mathbf{U}_{33}} \right), \quad (\text{B.7a})$$

$$\psi = \tan^{-1} \left(\frac{\mathbf{U}_{31}}{\sqrt{\mathbf{U}_{32}^2 + \mathbf{U}_{33}^2}} \right), \quad (\text{B.7b})$$

$$\varphi = \tan^{-1} \left(\frac{\mathbf{U}_{21}}{\mathbf{U}_{11}} \right). \quad (\text{B.7c})$$

The right quadrant of each angle is found by looking at the sign of the numerator and denominator.

B.1.2 Analytical Analysis of Error Propagation

In experiments the exact position of \mathbf{x}_n and \mathbf{y}_n cannot be determined exactly due to measurement uncertainties. Suppose that the measurement uncertainties in \mathbf{x}_n and \mathbf{y}_n are given by $\delta\mathbf{x}_n$ and $\delta\mathbf{y}_n$, so that the best mapping from $X + \delta X$ to $Y + \delta Y$ has to be found. The minimization problem (Equation B.1) changes to

$$E = \sqrt{\frac{1}{N} \sum_{n=1}^N w_n (\mathbf{U}[\mathbf{x}_n + \delta\mathbf{x}_n] - [\mathbf{y}_n + \delta\mathbf{y}_n])^2}, \quad (\text{B.8})$$

Since this equation is difficult to solve analytically and to compare with rotations found from Equation B.1 we simplify the problem by looking at the uncertainty in angular position of a single marker as shown in Figure B.2, e.g. we search for the unitary matrix \mathbf{U} which maps \mathbf{x} to $\mathbf{x} + \delta\mathbf{x}$

$$\mathbf{U}(\theta, \psi, \varphi) = \mathbf{U}_z(\varphi) \cdot \mathbf{U}_y(\psi) \cdot \mathbf{U}_x(\theta) \quad (\text{B.9})$$

$$= \begin{bmatrix} \cos \varphi \cos \psi & \cos \varphi \sin \psi \sin \theta - \sin \varphi \cos \theta & \cos \varphi \sin \psi \cos \theta + \sin \varphi \sin \theta \\ \sin \varphi \cos \psi & \sin \varphi \sin \psi \sin \theta + \cos \varphi \cos \theta & \sin \varphi \sin \psi \cos \theta - \cos \varphi \sin \theta \\ -\sin \psi & \cos \psi \sin \theta & \cos \psi \cos \theta \end{bmatrix}.$$

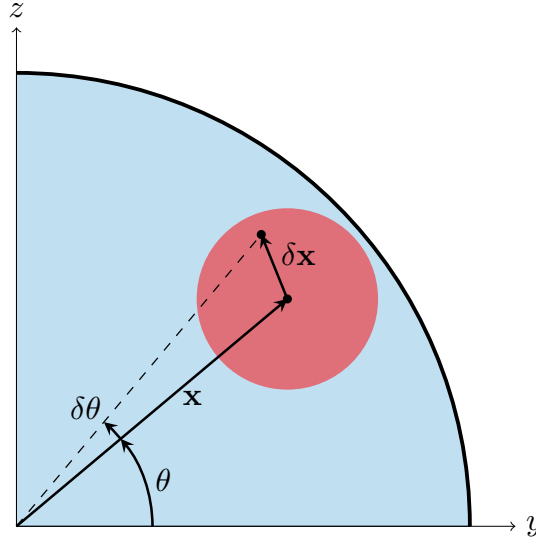


Figure B.2: Schematic representation of the angular uncertainty for a single marker. The region of uncertainty around the exact marker position, located at \mathbf{x} , is given by the red circle. The resulting uncertainty in angular position, in this case only shown for a rotation $\delta\theta$ around the x -axis, is found by using the linearized Kabsch algorithm to find the optimal rotation from \mathbf{x} to $\mathbf{x} + \delta\mathbf{x}$.

Assuming the rotations are small ($\theta = \delta\theta, \psi = \delta\psi, \varphi = \delta\varphi$), a Taylor analysis and removal of higher order terms simplifies this matrix to

$$\mathbf{U} = \begin{bmatrix} 1 & -\delta\varphi & \delta\psi \\ \delta\varphi & 1 & -\delta\theta \\ -\delta\psi & \delta\theta & 1 \end{bmatrix}. \quad (\text{B.10})$$

Solving the system of equations $\mathbf{U}\mathbf{x} = \mathbf{x} + \delta\mathbf{x}$, with $\mathbf{x} = (x, y, z)$ and $\delta\mathbf{x} = (x', y', z')$ for the different angles yields

$$\begin{bmatrix} 0 & z & -y \\ -z & 0 & x \\ y & -x & 0 \end{bmatrix} \begin{bmatrix} \delta\theta \\ \delta\psi \\ \delta\varphi \end{bmatrix} = \begin{bmatrix} x' \\ y' \\ z' \end{bmatrix} \quad (\text{B.11})$$

This system is degenerate since we solve for points on a surface. For given $\delta\theta$ this solutions for $\delta\psi$ and $\delta\varphi$ are

$$\delta\psi = \frac{\delta\theta y - z'}{x}, \quad (\text{B.12a})$$

$$\delta\varphi = \frac{\delta\theta z + y'}{x}. \quad (\text{B.12b})$$

From this equation it becomes clear that the measurement uncertainty in ψ and φ is proportional to the uncertainty in θ and inversely proportional to the x -coordinate. The variation in θ is determined by evaluation of $\sqrt{y'^2 + z'^2}$ with $\delta\psi = \delta\varphi = 0$, leading to

$$\delta\theta = \frac{\sqrt{y'^2 + z'^2}}{\sqrt{y^2 + z^2}}. \quad (\text{B.13})$$

This equation states that the measurement uncertainty in θ is proportional to the size of the perturbation and inversely proportional to the distance to the axis of rotation. On the surface of a sphere the x coordinate is dependent on the y and z coordinate and a given radius R via

$$x(y, z) = \sqrt{R^2 - y^2 - z^2}. \quad (\text{B.14})$$

Therefore the error in ψ and φ is large for small and large values of x , ie. points which are respectively close to the boundary and center in the projection of the sphere to the yz -plane. Please note that all uncertainties in angular position are dependent on the decomposition of \mathbf{U} in rotations around x -, y - and z -axis. Since the rotation around the x -axis θ is dominant over the rotations around the y - and z -axis in our experiment it is natural to express $\delta\psi$ and $\delta\varphi$ in terms of $\delta\theta$.

To investigate the order of magnitude of the uncertainty in angles we assume $x, y, z = \mathcal{O}(R)$ and $x', y', z' = \mathcal{O}(e)^7$. Substitution in Equations B.12 and B.13

⁷Since $\sqrt{(x+x')^2 + (y+y')^2 + (z+z')^2} = R \Rightarrow xx' + yy' + zz' = 0$ when neglecting higher order perturbations.

gives the scaling with respect to e and R

$$\delta\theta = \mathcal{O}\left(\frac{e}{R}\right), \quad (\text{B.15a})$$

$$\delta\psi = \mathcal{O}\left(\frac{e}{R}\right), \quad (\text{B.15b})$$

$$\delta\varphi = \mathcal{O}\left(\frac{e}{R}\right). \quad (\text{B.15c})$$

Substituting $R = 5 \text{ mm}$ and $e = 0.2 \text{ mm}$, typical values in our experiment gives the following uncertainty in the measured angles, $\delta\theta = \delta\psi = \delta\phi = \mathcal{O}(0.04)$.

Since θ is the dominant rotation we will restrict our analysis to the rotation around x -axis. Looking at the error made between a point in the initial configuration with angular position $\theta_i + \delta\theta_i$ and rotated configuration with angular position $\theta_r + \delta\theta_r$ we find, assuming $\mathcal{O}(\delta\theta_i) = \mathcal{O}(\delta\theta_r) = \mathcal{O}(\delta\theta) \propto \frac{e}{R}$, that the error in the rotation of a single marker $\delta\dot{\theta}_1$ is given by

$$\delta\dot{\theta}_1 = \sqrt{2\delta\theta^2} = \sqrt{2}\delta\theta \propto \frac{e}{R}. \quad (\text{B.16})$$

Addition of multiple points N on the sphere decreases the standard deviation with $N^{-0.5}$. A similar scaling holds for the averaging of multiple measurements M over which the final result is averaged. Therefore the uncertainty in the rotation as function of $\dot{\theta}_1$, N and M becomes

$$\delta\dot{\theta} = \frac{\delta\dot{\theta}_1}{\sqrt{NM}}. \quad (\text{B.17})$$

Division of this result by the absolute rotation $\dot{\theta}$ gives the relative error

$$\varepsilon = \frac{\delta\dot{\theta}}{\dot{\theta}} = \frac{\delta\dot{\theta}_1}{\dot{\theta}\sqrt{NM}} \propto \frac{e}{R\dot{\theta}\sqrt{NM}}. \quad (\text{B.18})$$

Please note that in this result the weighting function in the Kabsch algorithm is neglected. As observed from Equation B.12, points lying nearby origin in the yz -plane contribute more to the uncertainty. The use of a proper weighting function, for instance $w_i = \sqrt{y^2 + z^2}$, will reduce the uncertainty.

B.1.3 Numerical Analysis of Error Propagation

To get an idea whether the results obtained in Section B.1.2 are in agreement with reality, a numerical analysis is performed, comparing the angular rotations from Equation B.1 and B.8.

Numerical Setup

Consider a sphere with radius R as shown in Figure B.3. A camera views the particle in the y - z plane of a right-handed coordinate system. N markers are

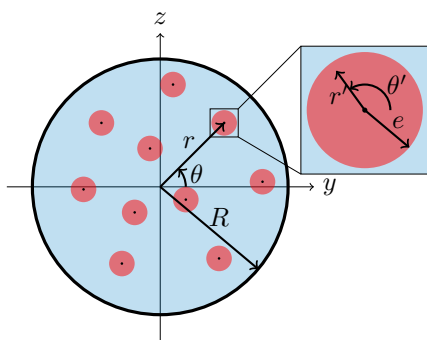


Figure B.3: Quantities involved in the simulation.

$\dot{\theta}$	0.001, 0.005, 0.01, 0.05, 0.1, 0.5, 1.0		
$e[\text{mm}]$	0.1, 0.2, 0.3, 0.4, 0.5		
$R[\text{mm}]$	5.0	N	2, 4, 6, 8, 10, 12, 14, 16
$R[\text{mm}]$	4.5	N	2, 4, 6, 8, 10, 12, 14
$R[\text{mm}]$	4.0	N	2, 4, 6, 8, 10, 12
$R[\text{mm}]$	3.5	N	2, 4, 6, 8, 10
$R[\text{mm}]$	3.0	N	2, 4, 6, 8
$R[\text{mm}]$	2.5	N	2, 4, 6
$R[\text{mm}]$	2.0	N	2, 4

Table B.1: Parameters used in the numerical analysis.

randomly initialized on the sphere using random numbers for both radial ($0 \leq r \leq R - R_b$) and angular coordinate ($0 \leq \theta < 2\pi$), satisfying a separation of at least $R_b = 0.5$ mm with the boundary and 1 mm with the other markers. A different perturbation is added to each marker using random numbers for the radial ($0 \leq r' \leq e$) as well the angular coordinates ($0 \leq \theta' < 2\pi$). Knowing that all markers are on a sphere with radius R the mapping from 2D to 3D coordinates is given by

$$(y, z) \mapsto (\sqrt{R^2 - y^2 - z^2}, y, z). \quad (\text{B.19})$$

The numerical analysis is performed using Python [Van Rossum and de Boer, 1991] and Python Scipy [Jones et al., 2001]. Processing of the data is done using Python Matplotlib [Hunter, 2007]. The script has the following approach

Exact solution ($e = 0$)

1. Initialize markers on 2D surface.
2. Perform mapping from 2D to 3D coordinates.
3. Rotate coordinates subsequently 100 times over an angle $\dot{\theta}$ using a rotation matrix \mathbf{U}_x .
4. Apply Kabsch-algorithm and return Euler-Cardan angles.

Perturbed solution ($e > 0$)

1. Initialize markers on 2D surface.
2. Perform mapping from 2D to 3D coordinates.
3. Rotate coordinates subsequently 100 times over an angle $\dot{\theta}$ using a rotation matrix \mathbf{U}_x .
4. Convert coordinates to 2D space.
5. Add a different perturbation to each marker at each time.
6. Convert perturbed 2D coordinates to 3D space.
7. Apply Kabsch-algorithm and return Euler-Cardan angles.

To avoid problems with markers ending up at the back of the sphere ($x < 0$) only rotations $\dot{\theta}$ around the x -axis are considered. Perturbations are added after

rotation since measurement uncertainties occur at the moment of observation and are not part of the physical behavior of the particle. This is also the reason why the random displacements of the markers have to be added to the 2D configuration.

The program is run for different radii R , rotations $\dot{\theta}$, measurement uncertainties e and number of markers on the sphere N . All configurations are listed in Table B.1. For every perturbation, the procedure shown above is repeated 10,000 times. Runs for $e = 0$ are performed once since this gives the exact solution to the minimization problem (B.1).

Error investigation

With the procedure described in the previous section, series containing $N_f = 99$ frames are obtained. For each frame the absolute value of the relative difference with the exact solution $|\frac{\Delta\theta}{\theta}|$ is determined and then averaged over the frames. This is done $N_{\text{err}} = 100$ times to obtain a smooth solution. The error ε therefore becomes

$$\varepsilon(R, e, \dot{\theta}, N, M) = \sum_{j=1}^{N_{\text{err}}=100} \sum_{i=1}^{N_f=99} \frac{\left| \frac{\delta\dot{\theta}_{ij}(R, e, \dot{\theta}, N, M)}{\dot{\theta}_{ij}} \right|}{N_{\text{err}} N_f}, \quad (\text{B.20})$$

where M denotes the amount of simulations over which $\delta\dot{\theta}$ is averaged.

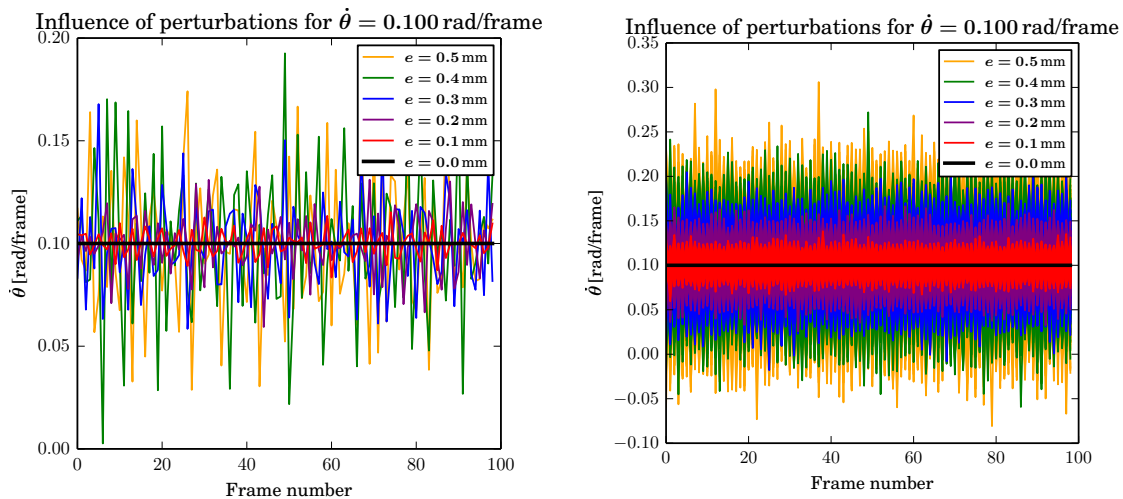
B.2 Results

This chapter is devoted to the results of the numerical analysis discussed in Section B.1.3. First the influence of measurement uncertainties on the measured rotation is discussed. Subsequently attention is paid to the reduction of the error defined by Equation B.20. At the end an overview of the separate results is given.

B.2.1 Influence of perturbations

Figure B.4 shows the influence of measurement uncertainties e on the measured angle of rotation $\dot{\theta}$. The black line corresponds to the exact solution and thereby proves that our implementation of the Kabsch Algorithm is correct.

For $e > 0$ however the exact solution is not obtained but the result moves around the exact solution. Figure B.4b, in which for each $e > 0$ 1000 lines are drawn, suggests that these fluctuations can be averaged out. This effect will be investigated in Section B.2.1. From both figures it becomes clear that the larger e , the larger the fluctuations around the exact value. This will be treated in more detail in Section B.2.1. The influence of angle of rotation $\dot{\theta}$, the size of the sphere R and the number of markers N , is not visible in Figure B.4, but is respectively discussed in Sections B.2.1, B.2.1 and B.2.1. Unless stated otherwise the results apply to a sphere with $R = 5$ mm to which $N = 8$ markers are applied.



(a) Influence of perturbations on the measured rotation $\dot{\theta}$. The black line indicates the exact solution. The larger the measurement uncertainty e , the bigger the deviation from the theoretical result.

(b) Influence of perturbations on the measured rotation $\dot{\theta}$. The black line indicates the exact solution. For each measurement uncertainty $e > 0$, 1000 results are drawn. Averaging multiple results will reduce the measurement error.

Figure B.4: Influence of perturbations on the measured rotation for single (a) and multiple results (b). Parameters used $R = 5$ mm, $N = 8$, $\dot{\theta} = 0.10$.

Averaging individual results M

As discussed in Section B.1.2 it is likely that taking the average of multiple measurements will reduce the error. In Figures B.5 and B.6 the results are shown for several values of e and $\dot{\theta}$. All lines have a slope of -0.5. This is in line with the result (B.18) of our analytical analysis stating

$$\varepsilon \propto M^{-0.5} \quad (\text{B.21})$$

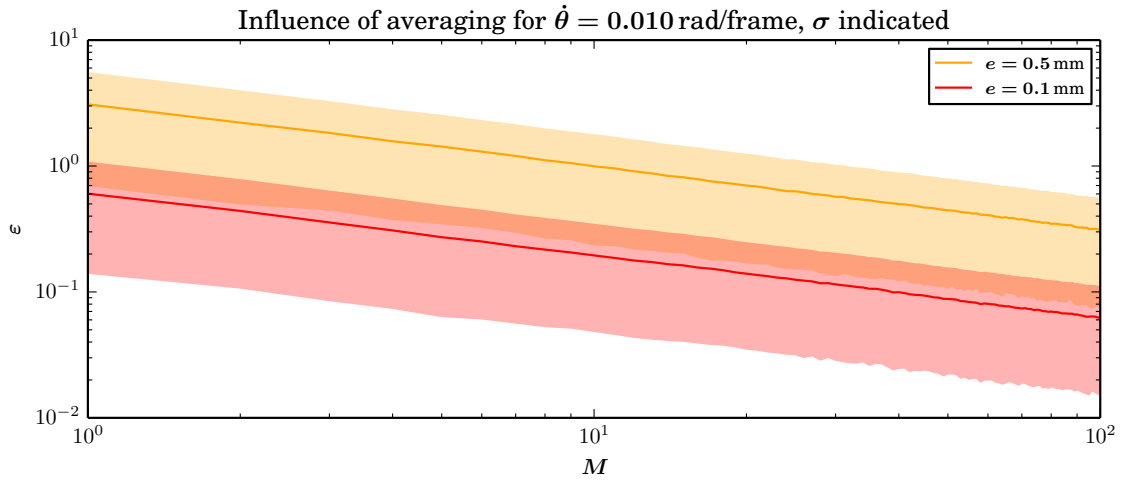


Figure B.5: Influence of averaging over multiple data series, with an indication of the standard-deviation σ in the modeled error. For each value of e , the line has a slope of -0.5. The standard-deviation in the error is of the same order as the error itself.

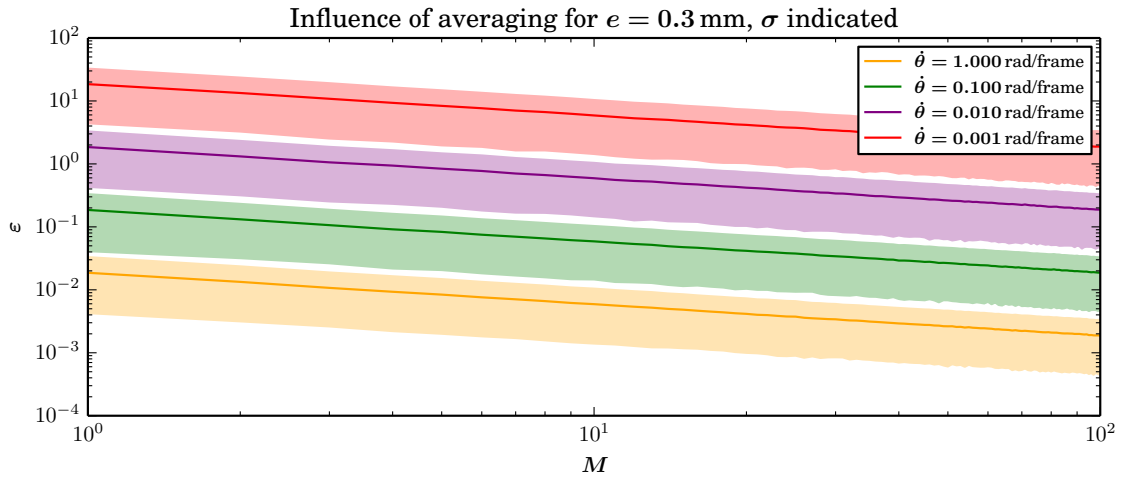


Figure B.6: Influence of averaging over multiple data series, with an indication of the standard-deviation σ in the modeled error ε . For each value of $\dot{\theta}$, the line has a slope of -0.5. The standard-deviation in the error is of the same order as the error itself.

Magnitude of error e

Equation B.18 states that the error in the measured angle is linearly proportional to the measurement uncertainty. Figure B.7 is in line with this conclusion and states that this relation holds also for large rotations. Therefore we have

$$\varepsilon \propto e \quad (\text{B.22})$$

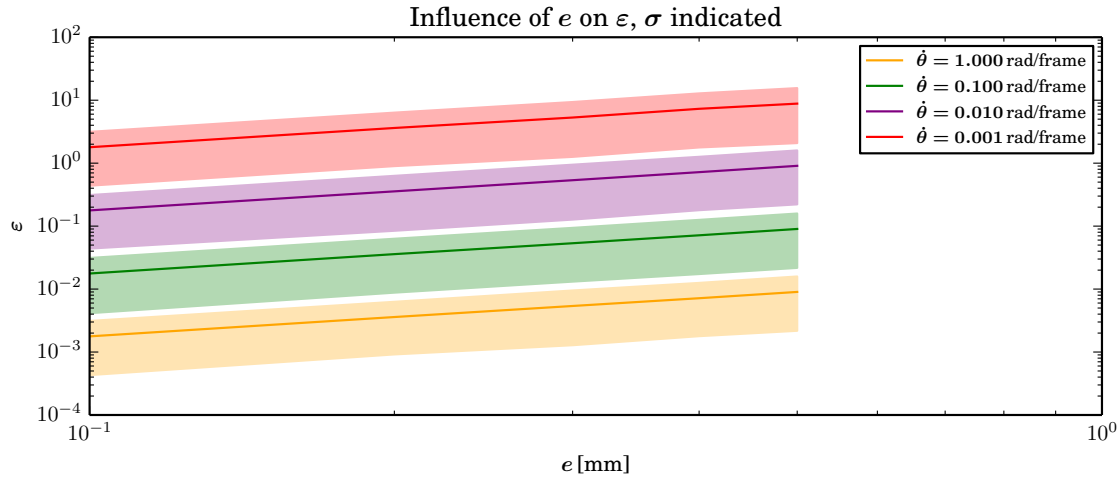


Figure B.7: Influence of the measurement uncertainty in the markers e , with an indication of the standard-deviation σ in the modeled error ε . Even for large values of $\dot{\theta}$ the line has a slope of 1. The standard-deviation in the error is of the same order as the error itself.

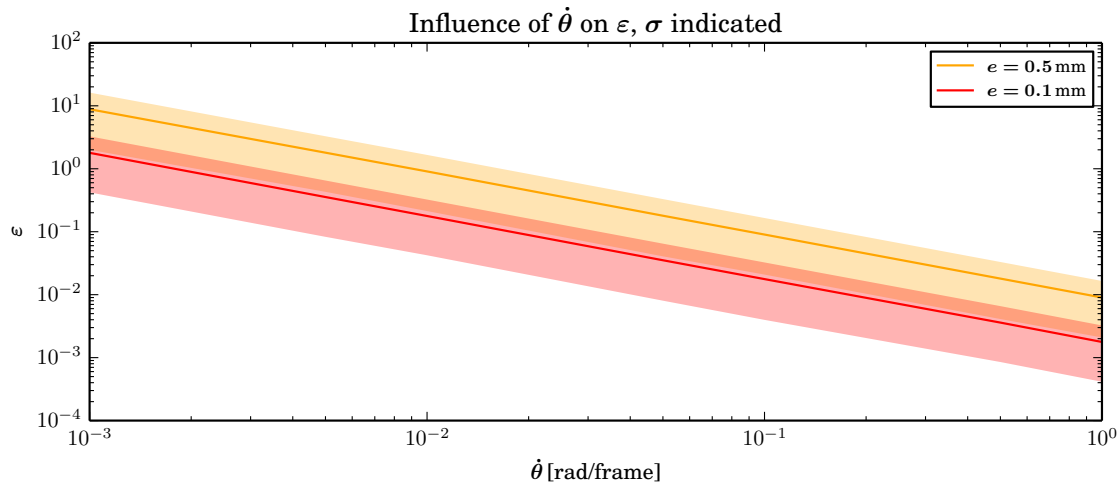


Figure B.8: Influence of the angle of rotation $\dot{\theta}$, with an indication of the standard-deviation σ on the modeled error ε . For all e and also for large values of $\dot{\theta}$ the line has a slope of -1. The standard-deviation in the error appears to be of the same order as the error itself.

Magnitude of rotation $\dot{\theta}$

From Figure B.8 it is observed that

$$\varepsilon \propto \dot{\theta}^{-1}. \quad (\text{B.23})$$

This result is valid for every modelled value of e and holds even for large rotations. This is in line with the result (B.18) from our analytical linearized analysis.

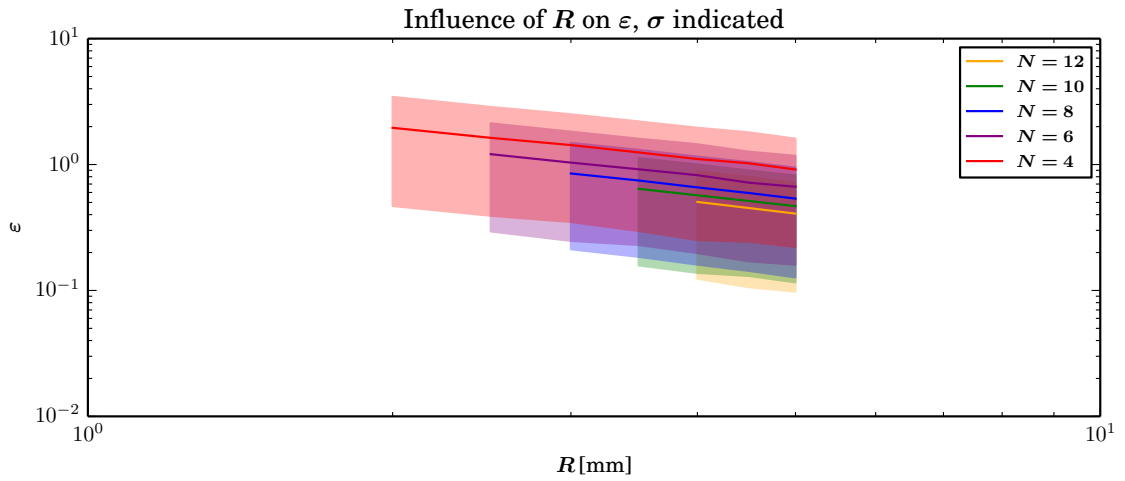


Figure B.9: Influence of the radius of the sphere R , with an indication of the standard-deviation σ on the modeled error ε . The slope of the line is dependent on the amount of markers applied to the sphere.

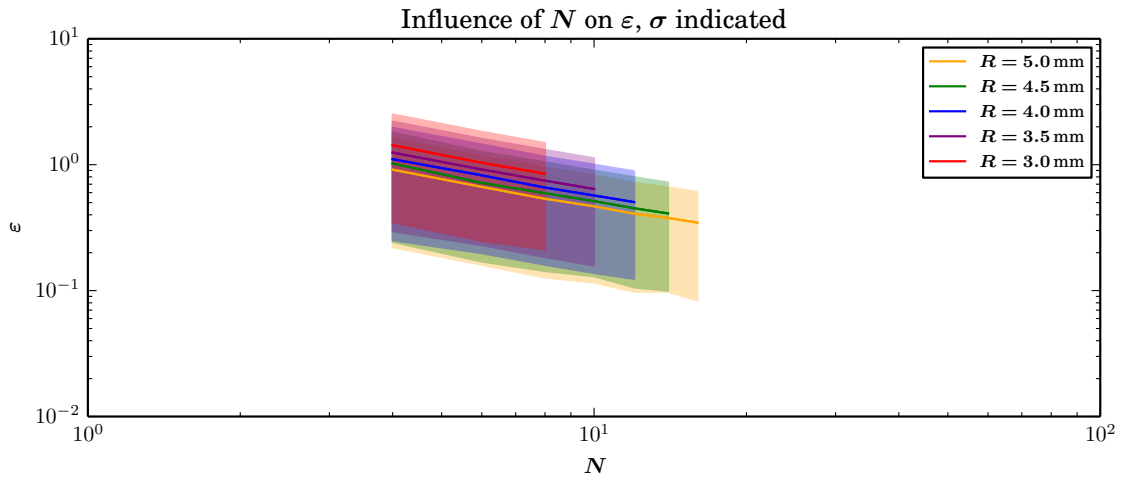


Figure B.10: Influence of the number of markers N applied to the sphere, with an indication of the standard-deviation σ on the modeled error ε . The slope of the line is dependent on the radius of the sphere.

N	4	6	8	10	12
Slope	-0.83	-0.85	-0.89	-0.88	-0.95

Table B.2: Values for the average slope of the results from Figure B.9.

R	2.0	3.0	3.5	4.0	5.0
Slope	–	-0.75	-0.72	-0.71	-0.69

Table B.3: Values for the average slope of the results from Figure B.10.

Radius of sphere R

From Figure B.9 one observes that the lines run not parallel to each other and that Kabsch Algorithm does not apply to a sphere with 2 markers on it. The slopes of the different lines are listed in Table B.2. The result from our analytical approximation, in which the error is inversely proportional to the radius, seems only to be valid if many markers are applied to the sphere.

Number of markers N

In Figure B.9 the influence of the number of markers N on the relative error ε is shown for different radii of the sphere. In this case the lines are run not parallel to each other but have a slightly different slope as listed in Table B.3. The value for $N = 2$ is erroneous and is therefore not taken into account. The values of the slope are higher than expected from the theoretical analysis in which $\varepsilon \propto N^{-0.5}$. This may be due the effect that markers lying close to the origin in the yz -plane contribute more to the error. Since the space around origin in the yz -plane is small, the relative influence of markers near the yz -plane origin reduces upon increasing the total number of markers.

B.2.2 Summary

In Table B.4 the results for the scaling of ε , as function of M , e , $\dot{\theta}$, R and N are given for both the analytical and numerical solution methods. For M , e and $\dot{\theta}$ the analytical solution equals the numerical solution. For R a discrepancy is observed, although this seems to disappear if many markers are applied to the sphere. The results for the number of markers shows a discrepancy between the two methods of calculation.

Analytical Result	Numerical Result
$\varepsilon \propto M^{-0.5}$	$\varepsilon \propto M^{-0.5}$
$\varepsilon \propto e$	$\varepsilon \propto e$
$\varepsilon \propto \dot{\theta}^{-1}$	$\varepsilon \propto \dot{\theta}^{-1}$
$\varepsilon \propto R^{-1}$	$\varepsilon \propto R^{-0.9}$
$\varepsilon \propto N^{-0.5}$	$\varepsilon \propto N^{-0.7}$

Table B.4: Comparison of analytical and numerical estimates for the scaling of the relative error. For the most parameters involved the results comply with each other. Only for the number of markers applied to the sphere a discrepancy is observed.

B.3 Conclusion

We found that the Kabsch Algorithm is sensitive to uncertainties in the position of the markers applied to a sphere. Although the standard-deviation in the observed errors was in all cases of the same order of the error itself, the scaling analysis proved to be similar to the analytical solution in which the rotation matrix was linearized. Therefore this analysis can be used to make a decent estimate of the error in the measured rotations of a sphere.

Bibliography

- Ballard, D. H. (1981). Generalizing the hough transform to detect arbitrary shapes. *Pattern recognition*, 13(2):111–122.
- Barnocky, G. and Davis, R. H. (1988). Elastohydrodynamic collision and rebound of spheres: Experimental verification. *Physics of Fluids*, 31:1324.
- Barnocky, G. and Davis, R. H. (1989). The influence of pressure-dependent density and viscosity on the elastohydrodynamic collision and rebound of two spheres. *Journal of Fluid Mechanics*, 209:501–519.
- Brenner, H. (1961). The slow motion of a sphere through a viscous fluid towards a plane surface. *Chemical engineering science*, 16(3):242–251.
- Breugem, W.-P. (2012). A second-order accurate immersed boundary method for fully resolved simulations of particle-laden flows. *Journal of Computational Physics*, 231(13):4469–4498.
- Costa, P., Boersma, B. J., Westerweel, J., and Breugem, W.-P. (2015). A collision model for fully-resolved simulations of flows laden with finite-size particles. *arXiv preprint arXiv:1506.01880*.
- Crowe, C. T., Schwarzkopf, J. D., Sommerfeld, M., and Tsuji, Y. (2011). *Multi-phase flows with droplets and particles*. CRC press.
- Davis, R. H., Serayssol, J.-M., and Hinch, E. (1986). Elastohydrodynamic collision of two spheres. *Journal of Fluid Mechanics*, 163:479–97.
- Derksen, J. (2011). Simulations of granular bed erosion due to laminar shear flow near the critical shields number. *Physics of Fluids (1994-present)*, 23(11):113303.
- Durán, O., Andreotti, B., and Claudin, P. (2012). Numerical simulation of turbulent sediment transport, from bed load to saltation. *Physics of Fluids (1994-present)*, 24(10):103306.
- Foerster, S. F., Louge, M. Y., Chang, H., and Allia, K. (1994). Measurements of the collision properties of small spheres. *Physics of Fluids*, 6:1108.
- Gatignol, R. (1983). The faxén formulas for a rigid particle in an unsteady non-uniform stokes-flow. *Journal de Mécanique théorique et appliquée*, 2(2):143–160.
- Gondret, P., Hallouin, E., Lance, M., and Petit, L. (1999). Experiments on the motion of a solid sphere toward a wall: From viscous dissipation to elastohydrodynamic bouncing. *Physics of Fluids*, 11:2803.
- Gondret, P., Lance, M., and Petit, L. (2002). Bouncing motion of spherical particles in fluids. *Physics of Fluids (1994-present)*, 14(2):643–652.

- Hunter, J. D. (2007). Matplotlib: A 2D graphics environment. *Computing In Science & Engineering*, 9(3):90–95.
- Jones, E., Oliphant, T., Peterson, P., et al. (2001). SciPy: Open source scientific tools for Python. <http://www.scipy.org/>.
- Joseph, G. and Hunt, M. (2004). Oblique particle–wall collisions in a liquid. *Journal of Fluid Mechanics*, 510(1):71–93.
- Joseph, G., Zenit, R., Hunt, M., and Rosenwinkel, A. (2001). Particle-wall collisions in a viscous fluid. *Journal of Fluid Mechanics*, 433:329–346.
- Kabsch, W. (1976). A solution for the best rotation to relate two sets of vectors. *Acta Crystallographica Section A: Crystal Physics, Diffraction, Theoretical and General Crystallography*, 32(5):922–923.
- Kabsch, W. (1978). A discussion of the solution for the best rotation to relate two sets of vectors. *Acta Crystallographica Section A: Crystal Physics, Diffraction, Theoretical and General Crystallography*, 34(5):827–828.
- Kempe, T., Vowinckel, B., and Fröhlich, J. (2014). On the relevance of collision modeling for interface-resolving simulations of sediment transport in open channel flow. *International Journal of Multiphase Flow*, 58:214–235.
- Klein, S., Gibert, M., Bérut, A., and Bodenschatz, E. (2013). Simultaneous 3d measurement of the translation and rotation of finite-size particles and the flow field in a fully developed turbulent water flow. *Measurement Science and Technology*, 24(2):024006.
- Legendre, D., Daniel, C., and Guiraud, P. (2005). Experimental study of a drop bouncing on a wall in a liquid. *Physics of Fluids (1994-present)*, 17(9):097105.
- Legendre, D., Zenit, R., Daniel, C., and Guiraud, P. (2006). A note on the modelling of the bouncing of spherical drops or solid spheres on a wall in viscous fluid. *Chemical engineering science*, 61(11):3543–3549.
- MATLAB (2014). *version 8.4.0.150421 (R2014b)*. The MathWorks Inc., Natick, Massachusetts.
- Maw, N., Barber, J., and Fawcett, J. (1976). The oblique impact of elastic spheres. *Wear*, 38(1):101–114.
- Maxey, M. R. and Riley, J. J. (1983). Equation of motion for a small rigid sphere in a nonuniform flow. *Physics of Fluids (1958-1988)*, 26(4):883–889.
- Millman, K. J. and Aivazis, M. (2011). Python for scientists and engineers. *Computing in Science & Engineering*, 13(2):9–12.
- Morris, J. F. (2009). A review of microstructure in concentrated suspensions and its implications for rheology and bulk flow. *Rheologica acta*, 48(8):909–923.
- Oliphant, T. E. (2007). Python for scientific computing. *Computing in Science & Engineering*, 9(3):10–20.

- Shields, A. (1936). Application of similarity principles and turbulence research to bed-load movement. Technical report, Soil Conservation Service.
- Subramanian, R. S. (2010). Drag on spherical particles and steady settling velocities. Available online at <http://www.clarkson.edu/subramanian/ch301/notes/index.htm>.
- Van Der Walt, S., Colbert, S. C., and Varoquaux, G. (2011). The numpy array: a structure for efficient numerical computation. *Computing in Science & Engineering*, 13(2):22–30.
- van Rossum, G. and de Boer, J. (1991). Interactively testing remote servers using the python programming language. *CWI Quarterly*, 4(4):283–303. <http://www.python.org/>.
- Walton, O. R. (1993). Numerical simulation of inelastic, frictional particle-particle interactions.
- Warncke, N. (2014). *Turbulent Particle Transport and its Effect on Flotation*. PhD thesis, Delft University of Technology.
- Not listed in this bibliography are the numerous pages of Wikipedia (wikipedia.org) I used to keep track of the different equations, notations, and phenomena.

